

# Understanding the microscopic processes that govern the charge-induced deformation of carbon nanotubes

Lars Pastewka,<sup>1,2,\*</sup> Pekka Koskinen,<sup>3,4</sup> Christian Elsässer,<sup>1,3</sup> and Michael Moseler<sup>1,2,3,†</sup>

<sup>1</sup>*Fraunhofer Institute for Mechanics of Materials, Wöhlerstraße 11, 79108 Freiburg, Germany*

<sup>2</sup>*Institute of Physics, University of Freiburg, Hermann-Herder-Straße 3, 79104 Freiburg, Germany*

<sup>3</sup>*Freiburg Materials Research Center, Stefan-Meier-Straße 21, 79104 Freiburg, Germany*

<sup>4</sup>*NanoScience Center, Department of Physics, 40014 University of Jyväskylä, Finland*

(Dated: October 2, 2009)

While carbon nanotubes have technological potential as actuators, the underlying actuation mechanisms remain poorly understood. We calculate charge-induced stresses and strains for electrochemical actuation of carbon nanotubes with different chiralities and defects, using density-functional theory and various tight-binding models. For a given deformation mode the concept of bonding and anti-bonding orbitals can be redefined depending on the sign of a differential band structure stress. We use this theoretical framework to analyse orbital contributions to the actuation. These show charge asymmetric behavior which is due to next-nearest-neighbor hopping, while Coulombic contributions account for approximately charge-symmetric isotropic deformations. In the typical case of a (10,10) tube strains around 0.1% with 1 nN force along the tube axis are obtained. Defects and functional groups have negligible influence on the actuation. In multi-wall tubes we find charge inversion on the inner tubes due to Friedel-type oscillations which could lead to a slight magnification of charge-induced strains. Finally, we consider photo-actuation of nanotubes and predict that transitions between van-Hove singularities can be expected to expand the tubes.

PACS numbers: 61.48.De,68.35.Gy,71.20.Tx,73.30.+y

## I. INTRODUCTION

When a new material is discovered, its first applications are usually of a passive nature: carbon nanotubes (CNTs)<sup>1,2</sup> have, for example, been used to reinforce polymers<sup>3</sup>, metals<sup>4</sup> and ceramics<sup>5</sup>. Meanwhile technological advances try to push CNTs forward as an active material, e.g. for electronic devices<sup>6</sup>. Another type of active application is their use as actuators. The stimulus leading to a size change of the overall actuator, which is believed to be mediated by carbon nanotubes, can be quite different: electrostatic<sup>7,8</sup>, chemical<sup>9</sup>, electrochemical<sup>10</sup> as well as optical<sup>11</sup> actuation have been reported.

Electrostatic actuators are CNT beams or hinges which can be deflected or rotated by an electric field. In the other cases the microscopic mechanisms are still under discussion. However, a change in lattice constant of the individual CNT was originally proposed<sup>10</sup> and later confirmed experimentally<sup>12</sup>. While initially electrochemical actuation was demonstrated by dipping a nanotube felt — also called “bucky-paper”<sup>10</sup> — into a liquid electrolyte, state-of-the-art devices usually consist of three components: carbon nanotubes are embedded in a polymer matrix which is impregnated with the electrolyte<sup>13</sup>. These devices are dry and can be operated at low voltages — making them competitive to piezo-electric elements operated at voltages of above 100 V. Photo-actuation was demonstrated for free-standing CNTs<sup>14</sup> as well as composites where large strains were observed upon infrared irradiation<sup>11,15–20</sup>. While the latter was linked to an alignment of individual tubes within the composite material, no explanation of the underlying mechanisms that trigger this alignment has been given so far.

Besides charge-induced changes of the lattice constant of individual tubes, the mutual interaction of tubes due to the presence of an electrolyte might also be important. Electrostatic double-layers mutually repel each other. This could lead to a swelling of the bucky-paper and can be described to a first approximation within the theory of Derjaguin, Landau, Verwey, and Overbeek (DLVO)<sup>21</sup>. Chemical reactions such as the dissociation of the electrolyte at the CNTs’ tips, where large electric fields are expected, might lead to the production of a gaseous species which also increases the volume. While it was shown that the individual tube changes its properties<sup>12</sup>, it is not yet clear whether this is the change that translates into a macroscopic size change of the actuator.

For photo-induced actuation other mechanisms are also conceivable. The actuation could be mediated by conversion of infrared radiation into heat. However, thermal effects have been found to be an order of magnitude smaller than the observed photo-actuation<sup>11</sup>. Here, we show that there is an intrinsic quantum-mechanical contribution to a size change upon irradiation (Sec. IX).

This article focuses on quantum-mechanical mechanisms leading to a change in lattice constant for individual CNTs in the case of electrochemical and optical actuation. Previous studies of these quantum-mechanisms have focused on electrochemical actuators<sup>22–24</sup> and, unfortunately, give contradicting results for apparently identical systems, a discrepancy which we resolve in Section VII. Our discussion starts by investigating the band structure of CNTs and identifying the contributions of different orbitals to the stress which the CNTs can exert when their size is confined (Sec. IV). This is suf-

ficient to describe the actuation using optical stimulus where the system stays charge neutral (Secs. V, VI and IX); however, it is not sufficient for electrochemical actuation. Here, Coulombic interactions on single tubes and local charge compensation due to the presence of the electrolyte needs to be considered as well (Sec. VII). Within this context, multi-wall tubes are also discussed (Sec. VIII).

The effect of strain and torsion on the electronic structure of CNTs has been discussed previously by several authors. White and Mintmire<sup>25,26</sup> used a simple  $\pi$ -orbital nearest-neighbor tight-binding model to derive an analytical expression for the density of states of CNTs around the Fermi level. This has been extended to the case of distorted CNTs by Yang and Han<sup>27</sup> by considering the change in nearest-neighbor hopping due to radial and axial strain. Accompanying their computational work, Verissimo-Alves and co-workers<sup>23</sup> derived an analytical model within the same picture but considered isotropic strain only. Gartstein and co-workers<sup>28,29</sup> developed a theory which also includes next-nearest-neighbor hopping integrals and all possible deformation modes which do not break the symmetry introduced by the underlying graphene lattice. In a similar approximation, Hartman and co-workers<sup>12</sup> computed the shift in phonon frequency due to electromechanical coupling which was experimentally compared to the shift of the Raman  $G$ -peak. The response of short isolated nanotubes was further investigated quantum-mechanically<sup>30</sup> and classically by assuming only electrostatic interaction and the CNT's elastic response<sup>31,32</sup>. Here, we approach the problem by starting with the electronic density of states in the independent electron approximation. We assess the validity of the above theories by comparing different levels of electronic structure theory.

A variety of literature for actuation of charged metals in contact with an electrolyte<sup>33</sup> already exists. We make reference to thermodynamic<sup>34,35</sup> and electronic structure<sup>36,37</sup> theories where appropriate.

## II. STRESS IN TIGHT-BINDING MODELS

As a motivation and an instructional example, we consider the stress in a nanotube within a non-orthogonal tight-binding model. Given Hamiltonian matrix elements  $H_{I\mu J\nu}$  and overlap matrix elements  $S_{I\mu J\nu}$  the generalized eigenvalue problem  $(\underline{H} - \epsilon \underline{S})\vec{C} = \vec{0}$  yields a set of eigenenergies  $\epsilon_n$  and corresponding eigenvectors  $C_{I\mu}^n$ <sup>38</sup>. The total energy is given by

$$E = E_{\text{TB}}^{\text{BS}} + E_{\text{rep}} = \sum_n \sum_{I\mu J\nu} C_{I\mu}^{n*} H_{I\mu J\nu} C_{J\nu}^n + E_{\text{rep}}, \quad (1)$$

where capital indices run over atoms while Greek indices run over orbitals for each atom. Usually the band structure component of the stress tensor  $\underline{\sigma}$  is computed from

the virial expression

$$V_0 \underline{\sigma}^{\text{BS}} = \sum_n \frac{1}{2} \sum_{I\mu J\nu} \vec{r}_{IJ} \otimes \left\{ \frac{\partial S_{I\mu J\nu}}{\partial \vec{r}_{IJ}} \epsilon_n - \frac{\partial H_{I\mu J\nu}}{\partial \vec{r}_{IJ}} \right\} C_{I\mu}^{n*} C_{J\nu}^n \quad (2)$$

where  $\vec{r}_{IJ}$  is the distance vector between atoms  $I$  and  $J$ .

Rewriting expression (2) in the form  $V_0 \underline{\sigma}^{\text{BS}} = \sum_n V_0 \delta \underline{\sigma}^n$  shows that the band structure component of  $\underline{\sigma}$  can be decomposed into orbital stresses  $\delta \underline{\sigma}^n$  which are occupied according to the charge state yielding the stress as a function of charge. Not surprisingly, such decomposition can be very useful for the analysis of microscopic actuation mechanisms. Of course, the decomposition seems to be limited to the special case of tight-binding models. Therefore, we seek in this article for a more model-independent definition of  $\delta \underline{\sigma}$ . In the following we will first show why the definition of stress is important for actuation and then generalize this definition for arbitrary deformation modes and arbitrary electronic structures theories.

## III. CHARGE-INDUCED DEFORMATIONS WITHIN THE LINEAR ELASTIC APPROXIMATION

Generally, the total electronic ground-state energy of a periodic system, as obtained for example from density functional theory (DFT), can be written as a function of the nuclei's relative coordinates  $\vec{x}_i$  and the vectors  $\vec{a}_i$  of the unit cell. The charge state of such a system is characterized by the chemical potential  $\mu$  giving a total energy function  $E(\{\vec{x}_i\}, \{\vec{a}_i\}, \mu)$ . If unperturbed, the system tries to find the minimum energy positions  $\vec{x}_i^{(0)}$  and unit cell  $\vec{a}_i^{(0)}$ . These positions are now perturbed by applying a set of small strains  $\gamma_i$  to the system. In the most general formulation, these strains transform the coordinates and the unit cell as  $\vec{x}_i = (\underline{1} + \underline{M}_x(\vec{\gamma}))\vec{x}_i^{(0)}$  and  $\vec{a}_i = (\underline{1} + \underline{M}_a(\vec{\gamma}))\vec{a}_i^{(0)}$ , respectively. Our goal is to extract the new minimum energy strains of the charged system at a chemical potential  $\mu$  from the uncharged case at a chemical potential  $\mu_0$ .

The Taylor expansion of the total energy around the neutral state zero strain  $\vec{\gamma} = 0$  yields

$$E(\vec{\gamma}, \mu) = E(0, \mu) + \left. \frac{\partial}{\partial \gamma_i} E(\vec{\gamma}, \mu) \right|_{\vec{\gamma}=0} \gamma_i + \frac{1}{2} \left. \frac{\partial^2}{\partial \gamma_i \partial \gamma_j} E(\vec{\gamma}, \mu) \right|_{\vec{\gamma}=0} \gamma_i \gamma_j + \mathcal{O}(\gamma^3), \quad (3)$$

where summation over repeated indices is assumed. In the uncharged case where  $\mu = \mu_0$  one finds  $\left. \frac{\partial}{\partial \gamma_i} E \right|_{\vec{\gamma}=0} = 0$  and  $\left. \frac{\partial^2}{\partial \gamma_i \partial \gamma_j} E \right|_{\vec{\gamma}=0}$  being positive definite because the system is in equilibrium. If the system's properties are now changed by raising or lowering the chemical potential  $\mu$ ,

the perturbed system finds a new equilibrium approximately at a strain

$$\bar{\gamma}^{\text{eq}}(\mu) = - \left[ \frac{\partial^2}{\partial \gamma_i \partial \gamma_j} E(\bar{\gamma}, \mu) \right]_{\bar{\gamma}=0}^{-1} \cdot \frac{\partial}{\partial \bar{\gamma}} E(\bar{\gamma}, \mu) \Big|_{\bar{\gamma}=0}. \quad (4)$$

Equation (4) can be regarded as a single step of a Newton-Raphson iteration starting from the charge neutral minimum energy configuration. In the same spirit as generalized forces we define a generalized stress  $\sigma_i$  for each deformation mode  $\gamma_i$  as

$$V_0 \sigma_i(\mu) = \frac{\partial}{\partial \gamma_i} E(\bar{\gamma}, \mu) \Big|_{\bar{\gamma}=0}, \quad (5)$$

where  $V_0$  is the volume in the unstrained case. Rewriting Eq. (4) yields

$$\bar{\gamma}^{\text{eq}}(\mu) = \underline{C}(\mu)^{-1} \cdot \bar{\sigma}(\mu) \quad (6)$$

where  $\underline{C}$  is a tensor of generalized elastic constants. Hence, by the knowledge of the first and second derivatives of  $E$  with respect to the strains in the system, the maximum strain (Eq. 4) and the blocking stress (Eq. 5) can be computed. Since the expansion of  $E(\bar{\gamma})$  is quadratic, the stress-strain relation for an arbitrary load of the actuator is linear. Note, that the usual stress in cartesian coordinates is included in the definition of the generalized stresses<sup>39</sup>. Using  $\underline{M}_x = 1$  and  $\underline{M}_a(\gamma) = \gamma \hat{x} \otimes \hat{y}$  the  $x$ - $y$ -component of the cartesian stress tensor is retrieved, while choosing  $\underline{M}_a(\gamma) = \gamma \underline{1}$  the generalized stress becomes the negative of the hydrostatic pressure.

In a CNT there are 3 macroscopic (axial, radial and torsional strain - see Fig. 1) and 2 microscopic (positions of the carbon atoms within the unit cell) deformation modes which do not break the symmetry of the underlying graphene lattice<sup>28</sup>. Here we consider only axial and radial strain and neglect the other degrees of freedom. Torsional strain is difficult to deal with in *ab-initio* calculations because the conventional unit cell length varies by orders of magnitude depending on torsion. Using analytical calculations within a  $\pi$ -orbital picture, Gartstein and co-workers<sup>28</sup> have found torsional deformations to be at least one order of magnitude smaller than radial and axial strain. In order to justify the neglect of the 2 microscopic deformation modes (which are known to be of importance for the correct elastic constants of graphene<sup>40</sup>) we perform additional simulations in which all atomic positions are relaxed.

With a tube aligned along the  $z$ -axis the transformation matrices for the axial and radial modes become

$$\underline{M}_x(\gamma_{\parallel}, \gamma_{\perp}) = 1 \quad \text{and} \quad \underline{M}_a(\gamma_{\parallel}, \gamma_{\perp}) = \begin{pmatrix} \gamma_{\perp} & 0 & 0 \\ 0 & \gamma_{\perp} & 0 \\ 0 & 0 & \gamma_{\parallel} \end{pmatrix}, \quad (7)$$

with axial strain  $\gamma_{\parallel}$  and radial strain  $\gamma_{\perp}$ . These quantities are related to the isotropic expansion  $2\gamma_0 = \gamma_{\parallel} + \gamma_{\perp}$

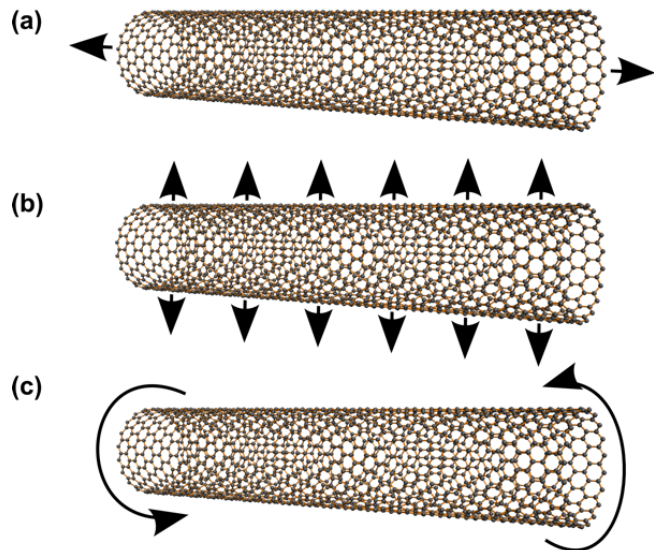


FIG. 1: (Color online) Deformation modes in a nanotube. (a) Axial deformation (denoted by  $\gamma_{\parallel}$ ), (b) radial deformation ( $\gamma_{\perp}$ ) and (c) torsional deformation ( $\eta$ ).

and anisotropic distortion  $2\gamma_1 = \gamma_{\parallel} - \gamma_{\perp}$ . The corresponding generalized stresses will be denoted by  $\sigma_{\parallel}$ ,  $\sigma_{\perp}$ ,  $\sigma_0$  and  $\sigma_1$ , respectively.

We would like to point out that there are more possible deformation modes in CNTs if symmetry breaking of the lattice is considered. While the methods described in this article should be applicable for a complete analysis of those, too, we expect that the long-wavelength deformations considered here are the dominant ones. Additionally, the anisotropic  $\gamma_1$  and torsional  $\tau$  deformation modes are volume conserving in linear order. The overall deformation of the macroscopic actuator — the actuation — is thus expected to be dominated by the isotropic  $\gamma_0$  deformation mode.

#### IV. ORBITAL CONTRIBUTION TO THE ACTUATION

The total energy  $E$  of a system is usually decomposed as<sup>41</sup>

$$E = E^{\text{BS}} + E^{\text{Coul}} + E^{\text{corr}}, \quad (8)$$

where the electronic (band structure) part can be written using the single-electron density of states  $g(\epsilon)$

$$E^{\text{BS}} = \int_{-\infty}^{\mu} d\epsilon \epsilon g(\epsilon). \quad (9)$$

Furthermore,  $E^{\text{Coul}}$  is the Coulomb interaction energy and  $E^{\text{corr}}$  a correction term leading to the correct total energy which depends on the respective level of theory.

In DFT, it contains the exchange and correlation energies while in tight-binding models these are approximated as a pair-wise repulsive potential. In the following discussion we ignore the Coulomb interaction; we reintroduce it later. We assume  $E^{\text{corr}}$  to be independent of the chemical potential  $\mu$ , an approximation already implicit in tight-binding models.

Taking the derivative of the band structure energy (Eq. 9) with respect to  $\gamma_i$  yields

$$\frac{\partial}{\partial \gamma_i} E^{\text{BS}} = \mu g(\mu) \frac{\partial}{\partial \gamma_i} \mu + \int_{-\infty}^{\mu} d\epsilon \epsilon \frac{\partial}{\partial \gamma_i} g(\epsilon), \quad (10)$$

where the first term is the derivative of the integral and captures the change in chemical potential due to strain, and the second term captures the change in band structure due to strain. Assuming furthermore that the total number of electrons in the system,

$$N_{\text{el}} = \int_{-\infty}^{\mu} d\epsilon g(\epsilon), \quad (11)$$

is constant, one finds

$$g(\mu) \frac{\partial}{\partial \gamma_i} \mu + \int_{-\infty}^{\mu} d\epsilon \frac{\partial}{\partial \gamma_i} g(\epsilon) = 0. \quad (12)$$

Substituting Eq. (12) into Eq. (10) leads to

$$\frac{\partial}{\partial \gamma_i} E^{\text{BS}} = \int_{-\infty}^{\mu} d\epsilon (\epsilon - \mu) \frac{\partial}{\partial \gamma_i} g(\epsilon). \quad (13)$$

whereas the second derivative of the energy  $E^{\text{BS}}$  with respect to  $\gamma_i$  and  $\gamma_j$  is given by

$$\begin{aligned} \frac{\partial^2}{\partial \gamma_i \partial \gamma_j} E^{\text{BS}} &= \int_{-\infty}^{\mu} d\epsilon (\epsilon - \mu) \frac{\partial^2}{\partial \gamma_i \partial \gamma_j} g(\epsilon) \\ &+ \frac{1}{g(\mu)} \int_{-\infty}^{\mu} d\epsilon \frac{\partial}{\partial \gamma_i} g(\epsilon) \int_{-\infty}^{\mu} d\epsilon \frac{\partial}{\partial \gamma_j} g(\epsilon). \end{aligned} \quad (14)$$

We would like to stress that these equations have been arrived at by assuming that the total number of electrons in the system is constant, i.e. it does not depend on strain. This is true for closed systems and has been implicitly assumed in previous studies of carbon nanotube actuation<sup>22–24,28,29</sup>. For optical stimulus this is a good assumption. In the case of electrochemical actuators, the system is always connected to an electron reservoir and thus the number of electrons is allowed to change. The constant electron number is merely an approximation, and valid only if the whole system has a capacity much smaller than the interfacial capacity of the nanotube, a

requirement that can be fulfilled by operating the actuator with a galvanostat.

Let us now decompose the density of states into contributions from different bands. We can write  $g(\epsilon) = \sum_k^{\text{partly filled}} g_k(\epsilon) + \sum_l^{\text{filled}} g_l(\epsilon)$  where the sum over  $l$  runs over bands which are completely filled. The contribution from the last sum becomes

$$\begin{aligned} \frac{\partial}{\partial \gamma_i} E_l^{\text{BS}} &= \int_{-\infty}^{\infty} d\epsilon (\epsilon - \mu) \frac{\partial}{\partial \gamma_i} g_l(\epsilon) \\ &= \frac{\partial}{\partial \gamma_i} E_l^{(0)} - \mu \frac{\partial}{\partial \gamma_i} N_l = \frac{\partial}{\partial \gamma_i} E_l^{(0)}, \end{aligned} \quad (15)$$

where  $N_l = \int d\epsilon g_l(\epsilon)$  is the total number of electrons in the respective band and thus constant with respect to  $\gamma_i$ . The energy  $E_l^{(0)} = \int_{-\infty}^{\infty} d\epsilon \epsilon g_l(\epsilon)$  is the total energy of band  $l$ . Not surprising, this means completely filled bands only contribute *elastically* to the overall actuation, i.e. they provide a restoring force that is independent of charging.

Electron or holes injected into bands change the band structure contribution to the stress  $\sigma_i^{\text{BS}} = \frac{1}{V_0} \frac{\partial}{\partial \gamma_i} E^{\text{BS}}$ . We define the *differential band structure stress*  $\delta\sigma_i$  as the change of stress  $\sigma_i^{\text{BS}}$  with respect to the number of electrons  $N_{\text{el}}$  in the system, i.e.

$$V_0 \delta\sigma_i = V_0 \frac{\partial}{\partial N_{\text{el}}} \sigma_i^{\text{BS}} = \frac{1}{g(\mu)} \frac{\partial^2}{\partial \mu \partial \gamma_i} E^{\text{BS}}. \quad (16)$$

Inserting Eq. (13) yields

$$V_0 \delta\sigma_i(\mu) = - \int_{-\infty}^{\mu} d\epsilon \frac{\partial}{\partial \gamma_i} g(\epsilon) \quad (17)$$

and furthermore invoking the constant electron number constraint Eq. (12) we find

$$V_0 \delta\sigma_i(\mu) = \frac{\partial}{\partial \gamma_i} \mu, \quad (18)$$

– a central equation of this article. Equation (18) gives the stress due to an *individual* electron injected into an orbital at the Fermi energy  $\mu$ . In this sense the differential band structure stress corresponds to the orbital resolved stress at the Fermi level of a finite system. Note that the total band structure stress is recovered by integrating over all energy levels, i.e.

$$\sigma_i^{\text{BS}}(\mu) = \int_{-\infty}^{\mu} d\epsilon g(\epsilon) \delta\sigma_i(\epsilon) \quad (19)$$

which is structurally identical to the band structure energy Eq. (9). Note that the *total* stress is given by  $\sigma = \sigma^{\text{BS}} + \sigma^{\text{Coul}} + \sigma^{\text{corr}}$  which sums to zero if the system is in equilibrium.

All equations above assume rigid bands with respect to charging, i.e. the density of states does not change when

the system is charged at constant strain. With respect to strain, the change in band structure is captured within linear response. In the following we will generally refer to this approximation as the rigid band approximation which we expect to work if the overall charge on the system is small. Implicitly, this also assumes that the CNTs charge homogeneously. Since the transition temperature for the formation of Peierls instabilities is two orders of magnitude below room temperature<sup>42</sup>, we expect similar transition temperatures for other instabilities and hence the rigid band approximation to be valid at room temperature for systems with a chemical potential close to the Fermi level. We additionally confirm the validity of this approach in Sec. VII where Coulomb interaction is explicitly included in a full NOTB model, and both, the rigid band approximation and the full NOTB model, agree in their results.

Note that Eq. (5) of the work of Umeno and co-worker (Ref. 36) is similar to our approach. It has been derived without reference to the electronic structure from thermodynamic considerations and is therefore a linear response approach. For charged bulk surfaces, such as for gold in Ref. 36, going beyond linear response is difficult because the electric field penetrates the surface and a rigid band approximation cannot be made.

It is now up to a certain microscopic model to establish the values of  $g(\epsilon)$ ,  $\frac{\partial}{\partial \gamma_i} g(\epsilon)$  and  $\frac{\partial^2}{\partial \gamma_i \partial \gamma_j} g(\epsilon)$ . Here, we compare the results of a  $\pi$ -orbital<sup>43</sup> zone-folding<sup>42,44,45</sup> model, non-orthogonal tight-binding<sup>38,46,47</sup> (NOTB) — with charge self-consistency<sup>48</sup> if appropriate — and DFT calculations with an extended local basis set<sup>49</sup>. While in the zone-folding model the derivatives of the density of states can be computed analytically, in NOTB and DFT we use a second-order finite differences approach with a step size of  $\Delta\gamma = 0.1\%$ . In these cases, the first and second derivative of  $E^{\text{corr}}$  is explicitly considered for the computation of the equilibrium strains  $\gamma^{\text{eq}}$ . It does however not change with the value of the chemical potential  $\mu$ .

### A. Strains in a $\pi$ -orbital zone-folding model

Considering next-nearest-neighbor hopping one finds that the band structure of a deformed CNT in the vicinity of the special “Dirac” points can be approximated by<sup>27–29</sup>

$$\epsilon_{\pm}(k) = \tau \pm \sum_{m=-\infty}^{\infty} |\xi_m(k)|. \quad (20)$$

where  $\xi_m(k)$  is due to nearest-neighbor hopping and we assume the next-nearest-neighbor hopping contribution  $\tau$  to have no dispersion and hence only shift the Fermi level. Here  $m$  runs over bands and the contribution of nearest-neighbor hopping is given by

$$|\xi_m(k)| = \sqrt{\Delta_m^2 + v_{\parallel}^2 k^2}. \quad (21)$$

The corresponding density of states per carbon atom can be written analytically<sup>25,27</sup>

$$g(\epsilon) = \frac{2}{lv_{\parallel}} \sum_{m=-\infty}^{\infty} \frac{|\epsilon - \tau|}{\sqrt{(\epsilon - \tau)^2 - \Delta_m^2}} \Theta(|\epsilon - \tau| - |\Delta_m|), \quad (22)$$

with  $l = \pi C / \sqrt{3} a_0$ . The quantity  $C a_0 = \sqrt{N^2 + M^2 + NM} a_0$  is the circumference<sup>50</sup> of a  $(N, M)$  tube,  $a_0$  the graphene lattice constant and  $\Theta(x)$  the step function. The gap-parameter

$$\Delta_m = v_{\perp} |K_m - A(\gamma_1 \sin 3\theta - \eta \cos 3\theta)| / a_0, \quad (23)$$

where  $\theta$  is the chiral angle as defined with respect to armchair tubes, i.e.  $\sin \theta = \frac{M-N}{2C}$ , and the effective Fermi velocities

$$v_{\parallel} = \frac{a_0 t_0}{2} \left\{ \sqrt{3} - A\gamma_{\parallel} \right\} \quad (24)$$

$$v_{\perp} = \frac{a_0 t_0}{2} \left\{ \sqrt{3} - A\gamma_{\perp} \right\}, \quad (25)$$

which give the slope of the Dirac cone in the graphene Brillouin zone, contain the influence of distortion. Furthermore, we use the abbreviations

$$A = \frac{\alpha a_0}{t_0}, \quad K_m = -\frac{2\pi(p+3m)}{3C}. \quad (26)$$

Here  $\alpha$  measures the strength of the modulation of the nearest-neighbor hopping matrix element  $t = t_0 - \alpha\delta$ , where  $t_0$  is the equilibrium hopping matrix element and  $\delta$  is the respective change in bond-length. The quantity  $K_m$  is the quantization condition for  $k$ -lines in the graphene Brillouin zone that give the  $m$ -th band of the CNT’s electronic structure, where  $p$  is the integer remainder of the division of  $N - M$  by 3.

The shift in Fermi level due to next-nearest-neighbor hopping is given by  $\tau = -3(u_0 - \beta\gamma_0)$  where  $u_0$  is the next-nearest-neighbor hopping matrix element and  $\beta$  its modulation with distance, i.e.  $u = u_0 - \beta\delta$ . A detailed derivation of these equations can be found in Appendix A.

The derivatives of the chemical potential  $\mu$  with respect to strain can be computed explicitly. Inserting Eq. (22) into Eq. (17) one finds for the isotropic differential band structure stress

$$V_0 \delta \sigma_0(\mu) = -\frac{\alpha a_0}{\sqrt{3}} \frac{\mu}{t_0} - 3\beta a_0, \quad (27)$$

which is independent of chirality. In Eq. (27) the Fermi level has been shifted to zero. This universality is due to the uniform scaling of bond lengths when the tubes are isotropically expanded and thus expected to hold true in more elaborate electronic structure models.

This model is referred to as  $\pi$ -2NH where we specifically use<sup>28</sup>  $a_0 = 2.461 \text{ \AA}$ ,  $t_0 = 2.5 \text{ eV}$ ,  $\alpha = 5 \text{ eV \AA}^{-1}$  and  $\beta = 0.5 \text{ eV \AA}^{-1}$ .

There is no intrinsic elastic contribution in the  $\pi$ -2NH model. In Refs. 28 and 29, these have been included using an established analytical elastic model for carbon nanotubes<sup>50</sup>. Here, we only display the contribution to stress.

### B. Strains in non-orthogonal tight-binding models

At a next level of approximation we choose to use NOTB<sup>38,46</sup> where the total energy expression has already been given in Eq. (1). Charge can be considered by adding a Coulomb interaction term

$$E_{\text{TB}}^{\text{Coul}} = \frac{1}{2} \sum_{IJ} G_{IJ}(r_{IJ}) \Delta q_I \Delta q_J \quad (28)$$

and solving the resulting equations self-consistently<sup>38,48</sup>. The Mulliken charge  $\Delta q_I$  is the charge in excess of the neutral atom  $I$  for which we assume a Gaussian shape<sup>51</sup>. This shape determines the short-range behavior of  $G_{IJ}(r_{IJ})$  while its long-range tail decays as  $r^{-1}$ . The diagonal elements  $G_{II}$  in the sum in Eq. (28) include a self-interaction term — the chemical hardness or Hubbard- $U$ .

Due to the discrete nature of the spectrum the chemical potential is given by  $\mu = \epsilon_n$  where  $\epsilon_n$  is the energy eigenvalue of the highest occupied orbital. Thus the differential band structure stress Eq. (18) becomes

$$V_0 \delta \sigma_i = \frac{\partial}{\partial \gamma_i} \epsilon_n, \quad (29)$$

where the energy eigenvalues can be explicitly expressed as

$$\epsilon_n = \sum_{I\mu J\nu} C_{I\mu}^{n*} H_{I\mu J\nu} C_{J\nu}^n. \quad (30)$$

Using the fact that the coefficients  $C_{I\mu}^n$  minimize the total band structure energy  $E_{\text{TB}}^{\text{BS}} = \sum_n^{\text{occ}} \epsilon_n$  it can be shown<sup>38</sup> that

$$\frac{\partial}{\partial C_{I\mu}^n} \epsilon_n = \frac{\partial}{\partial C_{I\mu}^n} E_{\text{TB}}^{\text{BS}} = \epsilon_n \frac{\partial}{\partial C_{I\mu}^n} \sum_{I\mu J\nu} C_{I\mu}^{n*} S_{I\mu J\nu} C_{J\nu}^n, \quad (31)$$

which yields

$$V_0 \delta \sigma_i = \sum_{I\mu J\nu} \left\{ C_{I\mu}^{n*} \frac{\partial H_{I\mu J\nu}}{\partial \gamma_i} C_{J\nu}^n + \epsilon_n \left( \frac{\partial C_{I\mu}^{n*}}{\partial \gamma_i} S_{I\mu J\nu} C_{J\nu}^n + C_{I\mu}^{n*} S_{I\mu J\nu} \frac{\partial C_{J\nu}^n}{\partial \gamma_i} \right) \right\}. \quad (32)$$

With the help of the orthogonality condition  $1 = \sum_{I\mu J\nu} C_{I\mu}^n S_{I\mu J\nu} C_{J\nu}^n$  this simplifies to

$$V_0 \delta \sigma_i = \sum_{I\mu J\nu} \left\{ \frac{\partial H_{I\mu J\nu}}{\partial \gamma_i} - \epsilon_n \frac{\partial S_{I\mu J\nu}}{\partial \gamma_i} \right\} C_{I\mu}^{n*} C_{J\nu}^n. \quad (33)$$

Choosing  $\underline{M}_a(\gamma) = \gamma \hat{x} \otimes \hat{y}$  yields the  $x$ - $y$  components of the stress tensor, i.e.

$$V_0 \delta \sigma_{xy} = \sum_{I\mu J\nu} r_{IJ}^y \left\{ \frac{\partial H_{I\mu J\nu}}{\partial r_{IJ}^x} - \epsilon_n \frac{\partial S_{I\mu J\nu}}{\partial r_{IJ}^x} \right\} C_{I\mu}^{n*} C_{J\nu}^n, \quad (34)$$

where we neglect three-center integrals such that  $H_{I\mu J\nu}(r_{IJ})$  and  $S_{I\mu J\nu}(r_{IJ})$  depend *only* on the relative position of atom  $I$  and atom  $J$ . Under these assumptions our theory thus yields Eq. (34) which is identical to the naïve definition of orbital resolved stress Eq. (2). From this derivation it also becomes clear, that if three-center integrals are included the orbital resolved stress cannot be defined as in Eqs. (2) and (34) anymore.

### C. Density functional theory calculations

Finally, we investigate our systems with DFT<sup>52</sup>. We use norm-conserving Troullier-Martins pseudopotentials<sup>53</sup> and a localized double- $\zeta$  basis including polarization orbitals, as implemented in the SIESTA code<sup>49</sup>. In all calculations involving only carbon atoms the local density approximation<sup>54</sup> as parametrized by Perdew and Zunger<sup>55</sup> is employed. When oxygen is present we use the generalized gradient approximation as parameterized by Perdew, Burke and Ernzerhof<sup>56</sup>.

In NOTB and DFT calculations 20 equally spaced  $k$ -points sample the full 1D-Brillouin zone and a Fermi broadening of 0.1 eV is used when relaxing the structures. For tubes with a large unit cell, i.e. in the case of defects or functionalization, we perform  $\Gamma$ -point calculations for relaxing the initial structures. Final densities of states are broadened by  $k_B \cdot 300 \text{ K} \approx 26 \text{ meV}$ .

## V. ACTUATION IN METALLIC AND SEMICONDUCTING TUBES

We start our study of single tube actuation by looking at the details of a metallic (10, 10) and a semiconducting (17, 0) tube, both of the same diameter. The density of states, shown in Fig. 2a, for the three microscopic models agrees around the Fermi level. Moving away from the Fermi level (i.e. away from the  $K$ -point in the graphene Brillouin zone) the predictions of the  $\pi$ -2NH model become worse as expected due to the underlying linearized graphene band structure. NOTB and DFT give almost identical density of states for the valence states, while the conduction states show different behavior. Unoccupied states are not considered in the tight-binding fitting procedure which leads to inferior accuracy of the conduction states as compared to DFT calculations<sup>46</sup>.

Turning to the differential band structure stress for the isotropic deformation mode  $\delta \sigma_0$  (Fig. 2b), one finds a behavior which almost perfectly matches the universal relationship Eq. (27). In NOTB, this relationship is followed

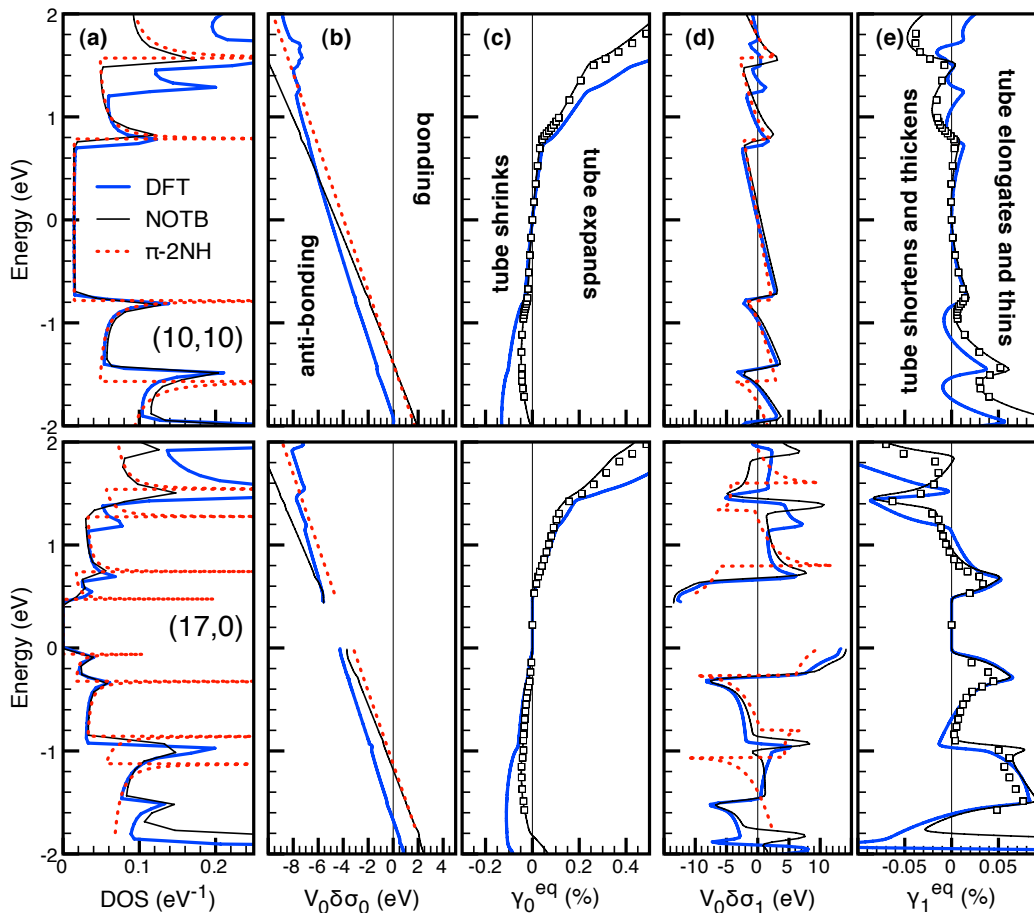


FIG. 2: (Color online) Actuator response of a metallic (10,10) (upper panel) and a semiconducting (17,0) (lower panel) nanotube. Thick solid lines show DFT results, thin solid lines results from NOTB calculations and broken lines results from a simple nearest-neighbor Hamiltonian, all within the linear stress-strain approximation, Eq. (3). Squares denote results from NOTB calculations with full relaxation, i.e. computations beyond the linear stress-strain approximation. From left to right the figures show (a) the density of states, (b) the isotropic differential band structure stress  $\delta\sigma_0$ , (c) the equilibrium isotropic strain  $\gamma_0^{\text{eq}}$ , (d) the anisotropic differential band structure stress  $\delta\sigma_1$  and (e) the equilibrium anisotropic strain  $\gamma_1^{\text{eq}}$  as a function of energy. The Fermi level is located at zero energy. Negative (positive) values of the differential band structure stress are termed *anti-bonding* (bonding) since they will expand (contract) the tube if populated.

over a window of approximately 2 eV while the DFT results show an earlier breakdown. However, around the Fermi level a perfect linear relationship is obtained in both cases. This holds also true for the semiconducting tubes just outside the band gap. The energy of transition between orbitals which contribute compressive stress and orbitals which contribute tensile stress can be attributed to next-nearest-neighbor hopping: it lifts the symmetry between the valence and conduction bands. If  $\beta = 0$  in the  $\pi$ -2NH model — giving a nearest-neighbor model — the curve becomes symmetric around the origin as the transition energy moves to the Fermi level.

The isotropic equilibrium strain  $\gamma_0^{\text{eq}}$  (Fig. 2c) shows distinct kinks at the van-Hove singularities (VHS). Since  $\delta\sigma_0$  is smooth these kinks are not related to the isotropic differential band structure stress. They are directly caused by the density of states contained in Eq. (19). An additional contribution from the anisotropic differen-

tial band structure stress via Eq. (6) is negligible as can be confirmed by relaxing only  $\gamma_0$ .

The open symbols in Figs. 2c and 2e denote NOTB calculations where all atomic coordinates have been relaxed for each charge state using the FIRE optimisation scheme<sup>57</sup>. These agree with calculations using approximation (3). This shows that the strain is small enough for a linear stress-strain relation to hold and relaxation of internal degrees of freedom is negligible.

The isotropic differential band structure stress  $\delta\sigma_0$  proposes a new definition of bonding and anti-bonding orbitals. Population of orbitals where  $\delta\sigma_0 < 0$  leads a volume expansion of the whole system while population of orbitals where  $\delta\sigma_0 > 0$  contracts the system. This behavior corresponds to what is typically expected of *anti-bonding* and *bonding* orbitals where usually changes in bond-lengths are monitored to determine the bonding character of a orbital. In terms of bonding and anti-

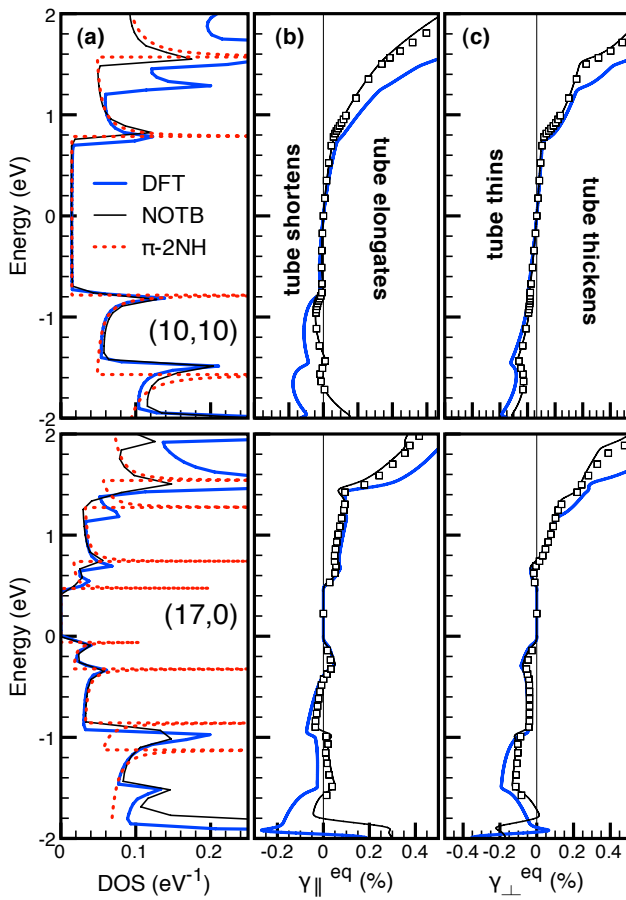


FIG. 3: (Color online) Actuator response of a metallic (10, 10) (upper panel) and a semiconducting (17, 0) (lower panel) nanotube as shown in Fig. 2. Here, all quantities are displayed for the axial ( $\parallel$ ) and radial ( $\perp$ ) instead of isotropic and anisotropic distortion modes.

bonding states the behavior of the isotropic equilibrium deformation  $\gamma_0^{\text{eq}}$  is straightforwardly explained. Starting from the charge-neutral case and lowering the chemical potential leads first to a de-population of anti-bonding states (the differential band structure stress in Fig. 2b is negative for these energies) — and thus a shrinking of the tube. For even lower chemical potentials the states become bonding and a de-population of those leads to tube expansion. When increasing the chemical potential from  $\mu = 0$  anti-bonding states are populated and this also leads to an expansion of the tube. Note that this discussion also holds for semiconducting tubes. Here, the valence band edge is always anti-bonding since a bandgap of around 3 eV would be needed to move the valence band edge to a bonding orbital.

The behavior with respect to anisotropic distortion is irregular. The differential stress  $\delta\sigma_1$  depends on the chirality of the tube and no universal relationship, like Eq. (27), exists. While isotropic distortion varies the Fermi velocities  $v_{\parallel}$  and  $v_{\perp}$  homogeneously, anisotropic distortion deforms the shape of the Dirac cone in the graphene

Brillouin zone. Furthermore, it displaces the minimum of the cone from the  $K$ -point if the tube is not armchair. Namely, upon isotropic expansion all matrix elements are scaled uniformly, while in anisotropic distortion the modulation depends on chirality. This is shown in Fig. 2d where besides having a different functional form the overall magnitude of the differential band structure stress  $\delta\sigma_1$  differs considerably between the armchair (10, 10) and zig-zag (17, 0) tube. This is also reflected in the equilibrium strain  $\gamma_1^{\text{eq}}$  as shown in Fig. 2e.

The  $\gamma_0$  and  $\gamma_1$  modes allow a decomposition of the tubes' deformations into principal modes with qualitatively distinct behavior. Natural for the description of actuation is the linear combination of these modes which leads to axial (elongation)  $\gamma_{\parallel}$  and radial (thickening)  $\gamma_{\perp}$  deformations of the tubes as shown in Fig. 3. The universal behavior of  $\delta\sigma_0$  is however obscured since the anisotropic mode influences both, axial and radial modes. However, the behavior of  $\gamma_{\parallel}$  and  $\gamma_{\perp}$  in the conduction bands is dominated by the isotropic  $\gamma_0$  mode. The valence bands are irregular and thus primarily dominated by the  $\gamma_1$  mode. In the case of the (10, 10) tube depopulation of valence states always leads to a radial contraction of the tube since this mode contains a linear combination of the  $\gamma_1$  mode and the inverse of the  $\gamma_1$  mode, leading to an almost monotonic behavior.

The force exerted by the tube can be computed straightforwardly. For the (10, 10) tube we find approximately  $-2$  nN and  $5$  nN axially at a charge of  $-0.05$  e/atom and  $0.05$  e/atom, respectively. The macroscopic stress is sensitive to the packing of the tubes. Assuming a hexagonal array of tubes and a tube-tube distance of  $2$  nm, one arrives at macroscopic axial stresses of between  $-0.2$  GPa and  $0.5$  GPa for charges between  $-0.05$  e/atom and  $0.05$  e/atom.

An overview of the size-dependence of the actuation behavior for armchair CNTs from (4, 4) to (10, 10) and zig-zag CNTs from (5, 0) to (18, 0) as probed using DFT is shown in Fig. 4 where the charge dependence of the 4 modes  $\gamma_0$ ,  $\gamma_1$ ,  $\gamma_{\parallel}$  and  $\gamma_{\perp}$  (individual columns) is displayed. As for the (10, 10) and (17, 0) tube the  $\gamma_0$ -mode is uniform for all tube sizes. The number of kinks in the actuator response — especially in  $\gamma_1^{\text{eq}}$  — increases with increasing tube diameter because the VHS move closer to each other. In other words, in the zone-folding picture the spacing between the quantization lines in the graphene Brillouin zone becomes smaller. For low charging all armchair tubes show qualitatively similar actuation because their density of states around the Fermi level is identical. The zig-zag tubes can be grouped according to the respective value of  $p$ , the integer remainder of the division of  $N - M$  by 3 (individual rows in Fig. 4). For metallic tubes where  $p = 0$ , the actuation around the Fermi level is identical for all tubes except for the small diameter (6, 0) tube, for which rehybridization takes place.

From experiments, interfacial capacities of up to  $10 \mu\text{F cm}^{-2}$  have been reported for single-wall CNTs<sup>10</sup>

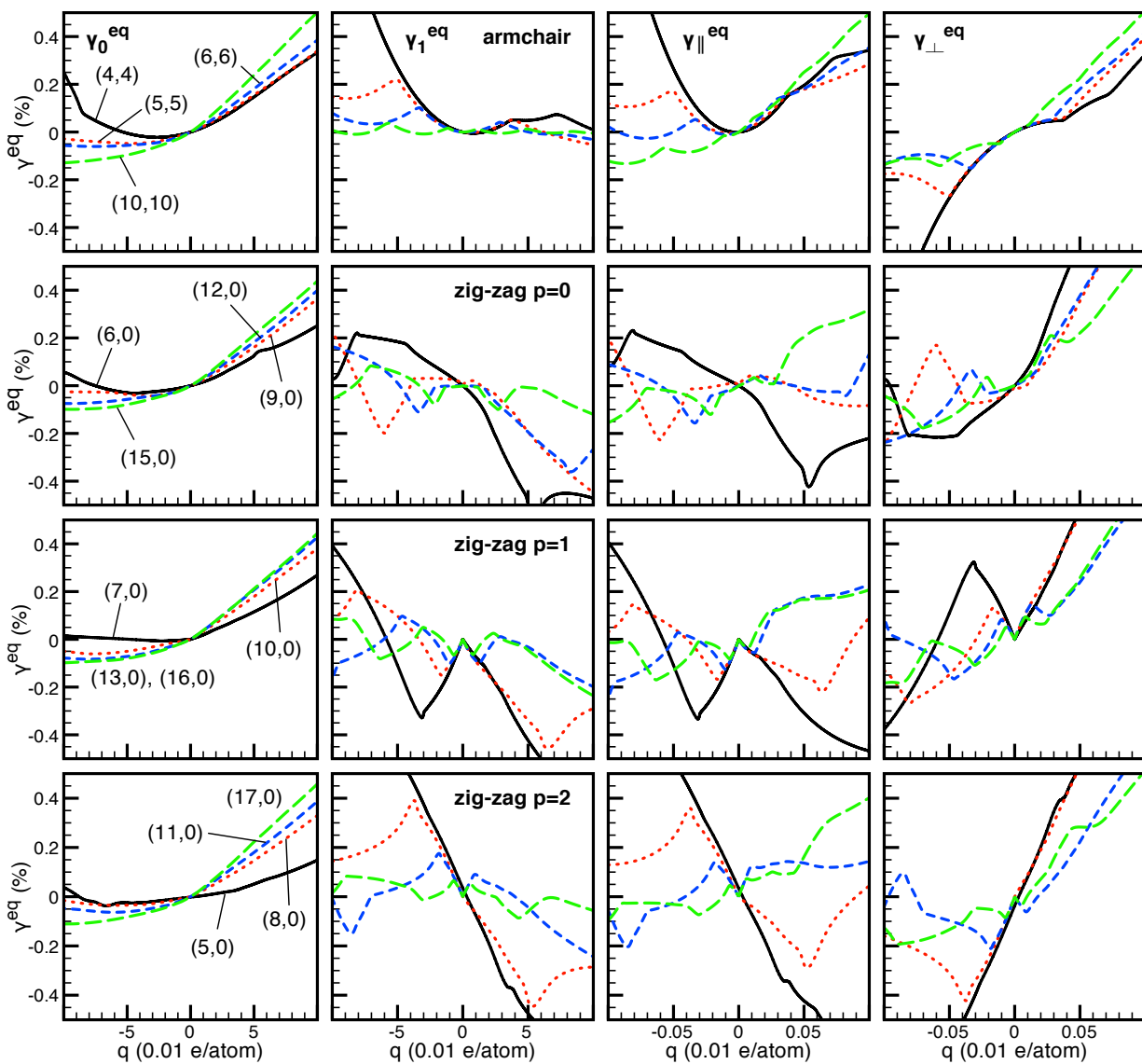


FIG. 4: (Color online) Isotropic (left panel), anisotropic (middle left panel), axial (middle right panel) and radial (right panel) strain of different carbon nanotubes upon charging where positive  $\gamma^{\text{eq}}$  means expansion, from DFT calculations in the rigid band approximation. The tubes are grouped into armchair  $(N, N)$  and zig-zag  $(N, 0)$  tubes for different values of  $p$  where  $p$  is the remainder of the division of  $N$  by 3. The isotropic behavior is similar for all tubes and approaches the same limit with increasing tube diameter.

and graphite<sup>58</sup>. Taking the surface area of a carbon atom occupied in an ideal graphene sheet one arrives at a capacity of roughly  $0.03 \text{ eV}^{-1}/\text{atom}$ . Hence, the range of charges displayed in Fig. 4 ( $-0.1 \text{ e/atom}$  to  $0.1 \text{ e/atom}$ ) corresponds to the maximum charging we expect in experiments when the system is driven at 3–4 V.

## VI. INFLUENCE OF FUNCTIONALIZATION ON TUBE ACTUATION

Carbon nanotubes as synthesized and purified by oxidation usually have 5% of carbon atoms located at a

defect site<sup>59</sup>. It is generally assumed that functional groups attach to these defects upon treatment in an oxygen plasma or acid (improving the tubes' solubility)<sup>60</sup>. Here we exemplarily analyse the influence of the common carboxyl group attached to a triple vacancy. We use five unit cells per functionalization for the semiconducting  $(11, 0)$  and the metallic  $(12, 0)$  tube giving a defect density similar to those found in experiments.

The relaxed configuration and Mulliken charges on the functional group are shown in Fig. 5. Between the  $(11, 0)$  and  $(12, 0)$  tube Mulliken charges differ by less than  $0.005e$ . In the following we discuss the  $(11, 0)$  tube. The density of states (Fig. 6a) shows that the vacancy

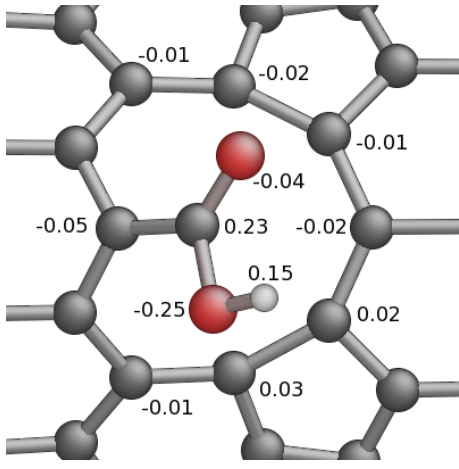


FIG. 5: (Color online) Relaxed atomic configuration of the carboxyl group and the triple vacancy. The numbers are Mulliken charges in units of  $-e$ .

introduces a gap state and decreases the band gap. The origin of the gap state is the vacancy’s dangling bond. Attachment of a carboxyl group increases the band gap and the density of the gap state. The contribution of the gap states to isotropic differential band structure stress  $\delta\sigma_0$  does not deviate from the universal behavior (Fig. 6b). It is however shifted to lower energies for both the triple vacancy and the functional group. This shift gives rise to a stronger actuator response as compared to the bare CNT (Fig. 6c). Due to this shift the orbitals have a stronger anti-bonding character which leads to stronger expansion upon population and stronger shrinking upon de-population. For anisotropic distortion, the gap-state for neither defect nor functional group has an influence on the actuation since its contribution to  $\delta\sigma_1$  vanishes (Fig. 6d). The overall behavior is irregular and the introduction of additional states due to the vacancy and the functional groups leave the overall variation in the differential band structure stress (Fig. 6d) and strain (Fig. 6e) mainly unchanged.

The density of states of the ideal metallic (12,0) is constant around the Fermi level. Introduction of the vacancy and functional group gives rise to distinct fluctuation in that region as shown in the lower panel of Fig. 6a. Furthermore a triple vacancy decreases the average density of states for the conduction bands. The differential band structure stress for isotropic deformation  $\delta\sigma_0$  follows the universal behavior and is independent of functionalization (Fig. 6b). No shift as in the case of the semiconducting tube is observed. The corresponding equilibrium strains  $\gamma_0^{\text{eq}}$  (Fig. 6c) are similar for the bare and the functionalized tube. A slightly weakened response is observed in the conduction band for a triple vacancy which can be attributed to the lower density of states. The stress  $\delta\gamma_1$  (Fig. 6d) for anisotropic distortion is similarly irregular to the semiconducting (11,0) case. The overall strain response  $\gamma_1^{\text{eq}}$  (Fig. 6e) is therefore similar to the ideal tube case.

## VII. COULOMBIC CONTRIBUTION TO THE ACTUATION

Previous sections discussed the change in band structure under strain ignoring all Coulombic effects which in reality also contribute to the overall actuation. In the case of electrochemical actuators<sup>10</sup> the individual carbon nanotubes are charged. This charge is compensated by ions drifting to the surface of the CNTs forming the dielectric double-layer<sup>21</sup>. Due to temperature fluctuations, the positions of the compensating charges are not fixed; however, on average the charges are well localized as described by Poisson-Boltzmann theory<sup>21</sup>, for example.

We present two different approaches to model the actuator including Coulomb interaction – both based on NOTB. First, we include a model of the dielectric double-layer (which we model as a uniformly charged cylindrical shell) into a full NOTB model where the Coulomb interaction is computed between all atoms as given in Eq. (28). Second, we use the rigid-band approximation and approximate the Coulomb interaction by the energy expression for a cylindrical capacitor. The second approach has the advantage that solvent effects on the dielectric constant can be incorporated in a mean-field sense. Also, the underlying band structure can be obtained from full DFT calculations in the latter case.

In full NOTB, we model the dielectric double-layer in a mean-field spirit as a uniformly charged cylindrical shell. Because of Gauss’ law<sup>61</sup> its radial character is not important unless the charges on the carbon atoms overlap with the double-layer. Hence, the double-layer’s charge distribution is given by (see inset in Fig. 7b for an illustration)

$$\rho(x, y, z) = \frac{Q}{2\pi r_0 l_z} \delta(\sqrt{x^2 + y^2} - r_0) - \frac{Q}{l_x l_y l_z} \quad (35)$$

which can be regarded as a cylindrical 2D-jellium. Here,  $r_0$  is the cylinder radius and  $Q$  the total charge in the unit cell with dimensions  $l_x$ ,  $l_y$  and  $l_z$ . The latter term compensates the cylinder’s charge and is cancelled by the 3D-jellium background implicit in the Ewald sum<sup>62</sup> which we use in our calculations. The solution of Poisson’s equation with the appropriate periodic boundary conditions (see Appendix B) is given by

$$\phi(\vec{r}) = -\frac{4\pi Q}{V} \sum_{G_x, G_y \neq 0; G_z = 0} \frac{J_0(Gr_0)}{G^2} e^{i\vec{G} \cdot \vec{r}} \quad (36)$$

where  $J_0$  is the Bessel function of the first kind and zeroth order. During relaxation, the cylinder radius is always kept at a constant distance  $d$  from the outer CNT wall. This effective solution model is implemented straightforwardly in NOTB. In plane-wave or real-space DFT calculations the electron affinity of the cylinder depends on its width. The delta-function approach used here would hence lead to electrons “spilling” from the system which accumulate on the cylinder when it is positively charged.

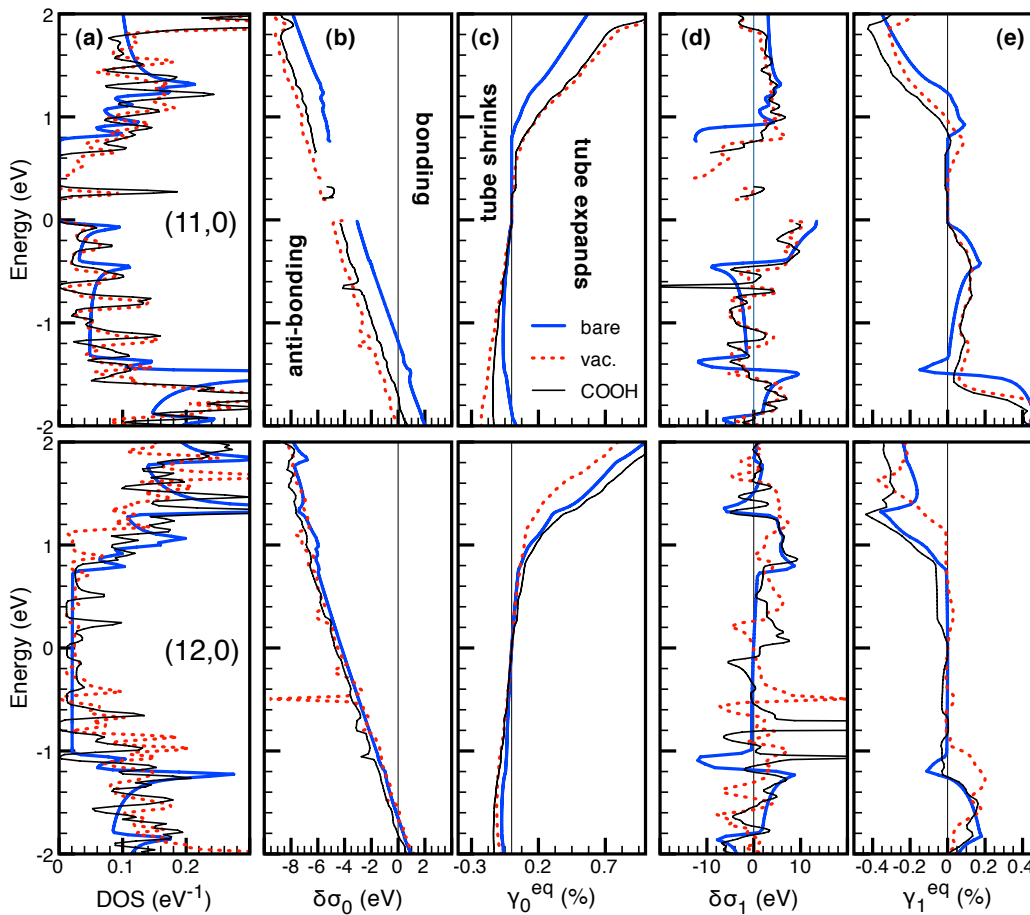


FIG. 6: (Color online) Actuator response of functionalized semiconducting (11,0) (upper panel) and metallic (12,0) (lower panel) CNTs computed within DFT and the rigid band approximation. Thick solid lines show results for unfunctionalized tubes, while broken lines and light solid lines are results for tubes with a triple vacancy and an attached carboxyl group, respectively. From left to right the figures show (a) the density of states, (b) the isotropic differential band structure stress  $\delta\sigma_0$ , (c) the anisotropic differential band structure stress  $\delta\sigma_1$ , (d) the equilibrium isotropic strain  $\gamma_0^{\text{eq}}$  and (e) the equilibrium anisotropic strain  $\gamma_1^{\text{eq}}$  as a function of energy.

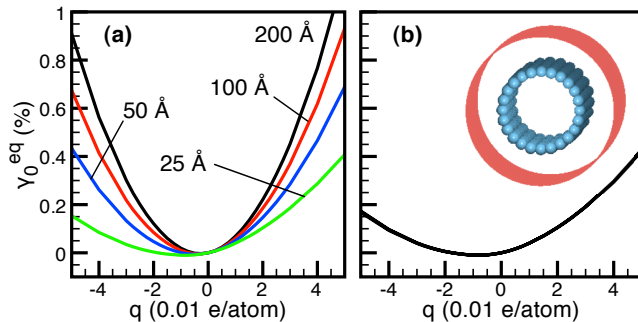


FIG. 7: (Color online) Influence of the unit cell size on the actuator strength shown for a (10,10) carbon nanotube from NOTB calculations. (a) Charge compensation using a 3D-Jellium model. (b) Charge compensation using a homogeneously charged cylindrical 2D-jellium. In direction perpendicular to the tube axis, the unit cell was chosen to be square with the side length given in the graph. In panel (b) all unit cell sizes fall exactly on top of each other. Lines connect calculated points.

Our approach is fundamentally different to earlier work on carbon nanotube actuation<sup>22–24</sup>, where charge compensation was achieved using a 3D-jellium which smears the compensating charge over the whole unit cell. Such a jellium is obtained by cancelling the zero-wavelength contribution in Ewald summation<sup>62</sup>. It leads to the following physical problems. First, the charges on individual tubes in the periodic assembly are not screened — this allows the tubes to interact electrostatically. Second, the self-energy of the 3D-jellium contributes to volume expansion. The total actuation therefore depends on the density of the 3D-jellium which in return depends on the choice of unit cell size perpendicular to the tube. Figure 7 demonstrates this effect for NOTB calculations and shows that for the compensating cylindrical jellium shell no such dependence is observed because the Coulombic interaction between different tubes is screened and the 3D-jellium density is constant. This also explains the apparently contradicting results of Refs. 22, 23 and 24: the size of the unit cell was simply chosen differently.

While Sun and co-workers<sup>24</sup> make a strong argument that their 3D-Jellium calculations are applicable to carbon-nanotube intercalation compounds, the validity in the case of a double-layer is questionable.

In the rigid band model, approximation (4), Coulombic effects can be included using a cylindrical capacitor whose capacitance and total electrostatic energy are given by

$$C = 2\pi\epsilon \frac{(1 + \gamma_{\parallel})l_z}{\ln\left(1 + \frac{d}{(1 + \gamma_{\perp})R}\right)} \quad \text{and} \quad E^{\text{Coul}} = \frac{Q^2}{2C}. \quad (37)$$

Here  $Q$  is the total charge in a cell of length  $l_z$ ,  $R$  the CNT's radius,  $d$  the double-layer distance, and  $\epsilon$  the constant of permittivity of the respective medium. Note that in the NOTB model the relative permittivity is set to unity since other choices would involve spurious interface charges. In the rigid band model the relative permittivity  $\epsilon_r$  of the medium can be included. The total energy has also a Coulombic self-energy contribution; in NOTB this is modeled by a single chemical hardness per atom<sup>38,48</sup>. While this self-energy contributes to the total capacitance of such a device, it only weakly depends on strain and is thus negligible.

Figure 8 shows the actuator response of a (10, 10) CNT including Coulombic contributions where we compare results of a full NOTB calculation using the cylinder model, Eq. (35), with an approximate computation using only rigid bands and the capacitor model Eq. (37). We use a distance  $d$  of 4 Å between CNT and double-layer in both cases. Both models show good agreement. Small differences can be attributed to the distance-dependence of the self-energy and the breakdown of a linear stress-strain relation. As a reference we also display the results without Coulomb interaction for which the dielectric constant becomes effectively  $\epsilon_r \rightarrow \infty$ . For solvents it is usually assumed that the dielectric constant in the vicinity of solvated ions saturates below its bulk value. The specific value is around  $\epsilon_r = 5$  for water or methanol<sup>63</sup>. Using this dielectric constant, quantum-mechanical and electrostatic actuation are similar in magnitude, while in the  $\epsilon_r = 1$  case electrostatics dominates the overall response (see Fig. 8). For electron injection ( $q > 0$ ) the quantum response is very pronounced and thus becomes the major driving force at  $\epsilon_r = 5$  for the isotropic  $\gamma_0$  mode. In contrast, for hole injection ( $q < 0$ ) the quantum response is almost negligible and thus electrostatics dominates the actuator behavior. Going to charges well above the displayed 0.1 e/atom electrostatics becomes the dominant source of actuation for both, electrons and holes. The anisotropic  $\gamma_1$  mode only weakly depends on the electrostatic interaction. In the  $\epsilon_r = 5$  case the curve almost ideally follows the non-interacting behavior at  $\epsilon_r \rightarrow \infty$ .

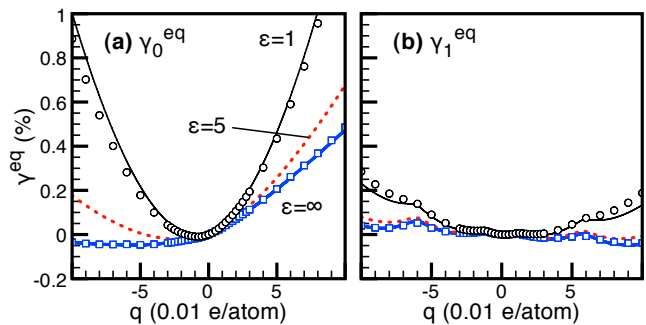


FIG. 8: (Color online) Actuator response of a (10, 10) carbon nanotube including Coulombic contributions. The figure shows the response of (a) isotropic  $\gamma_0^{\text{eq}}$  (b) and anisotropic  $\gamma_1^{\text{eq}}$  modes using full NOTB calculations with cylindrical charge compensation (symbols) and NOTB calculations within the rigid band approximation and a simple capacitor model (37) for the Coulomb energy (lines). The response for an effective dielectric constant of  $\epsilon_r = 5$  as expected for water is shown within the NOTB rigid band model only. The CNT double-layer distance  $d$  is 4 Å.

## VIII. ACTUATION AND CHARGE TRANSFER FOR MULTI-WALL TUBES

The picture employed above changes for multi-wall tubes since the rigid band approximation breaks down. Depending on the outer tube's ability to screen an electric field charges accumulate within multi-wall tubes. This can be probed with the NOTB double-layer model.

Figure 9a shows the charge per wall atom on the different walls of a (15, 15) – (10, 10) double-wall and a (15, 15) – (10, 10) – (5, 5) triple-wall CNT as a function of total charge per outer wall atom. Thus, we compare responses for the same charge per surface area — i.e. the charge per atom differs from system to system. The inner walls of the double and triple-wall tube acquire charges. For low charging these have the same sign and are thus due to the evanescent field. Above 0.05 e/atom the charge on the inner tube changes sign indicative of a Friedel-type oscillation. In the triple-wall case the inner tube is always negatively charged which indicates an increased electron affinity for small diameter tubes. The screening effect of the outer tube is overestimated in NOTB since in a minimal basis set atoms cannot polarize. The magnitude of these values has thus to be regarded as a lower limit. The right panel of Fig. 9 compares a double-wall tube where the inner wall is a metallic (15, 0) with a double wall tube where the inner wall is a semiconducting (14, 0) tube. It is noticeable that the charge transfer to the semiconducting inner wall is zero as long as the chemical potential is within the band gap. At the onset of charge transfer the charge on the inner wall has the opposite sign of the charge on the outer wall.

The overall actuation (shown in Fig. 9b) is lower than the corresponding single-walled tube. In our supercell calculations the walls are rigidly coupled i.e. the inner

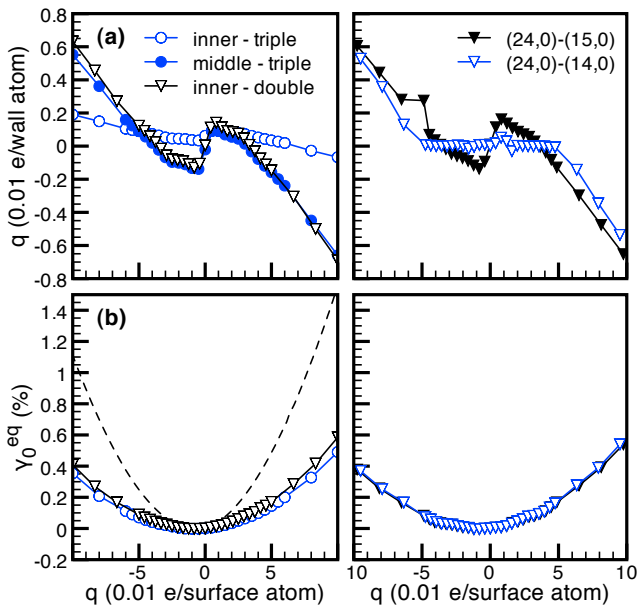


FIG. 9: (Color online) Charging and actuator response of a (15, 15) – (10, 10) double ( $\nabla$ ) and a (15, 15) – (10, 10) – (5, 5) triple-wall ( $\circ$ ) tube. (a) Charges on the inner walls of the CNTs as a function of charge per surface atom. (b) Actuator response upon charging. The broken line shows the response for a (15, 15) single wall tube. The charge response is displayed as charge per atom on the respective inner tube .

tubes has to be scaled according to the elongation of the outer one. In reality, the tubes are more weakly coupled via van-der-Waals interactions. The behavior is therefore determined by the frictional drag of the outer tube on the inner ones. Since the force of sliding the different walls against each other is rather small<sup>64,65</sup>, the results of Fig. 9b represent a lower limit for the outer tube actuation, because the inner tubes stick to the outer ones and hinder their motion. With no inter-tube sticking, charge inversion due to Friedel oscillations could even amplify the charge on the outer tube by a small amount leading to a slight increase in actuator response. No differences are observed between the metallic and semiconducting inner tubes because the charge transfer on these tubes is negligible.

## IX. ABOUT PHOTO-INDUCED ACTUATION

Exposure of carbon nanotubes to radiation leads to the formation of excitons<sup>66</sup>. Perturbation theory predicts that the most dominant transition is between VHS in the valence and conduction band because of their large density of states<sup>67–69</sup>. We discuss the density of states of the (17, 0) CNT shown in Fig. 2. Taking an electron from the highest occupied VHS and placing it into the lowest unoccupied VHS corresponds to an excitation energy of approximately 1.5 eV – an energy that can be provided by near infrared radiation. The overall system stays charge

neutral. Thus the charge neutrality assumption leading to the expressions of Sec. IV is fulfilled. Electrons from the highest occupied VHS have a negligible contribution to the overall stress for volume deformation and a negative contribution for anisotropic deformation. When an electron is promoted to the unoccupied VHS these contributions change. In the anisotropic case, expansion already occurs when the electron is taken from the highest occupied VHS because a bonding state is depleted. In the lowest unoccupied VHS the excited electron occupies a bonding state, further amplifying the effect. The tube expands anisotropically and isotropically. For other types of tubes the discussion continues along a similar path. While anisotropic deformations depend on tube chirality, the volume response is universal owing to Eq. (27). However, the actual magnitude of the deformation also depends on the radiation intensity and the lifetime of the excitation.

An analytic expression for the isotropic radiation-induced band structure stress can be given within the  $\pi$ -2NH model. The VHS are located at energies  $\pm\Delta_m$  as given in Eq. (23). Let  $n$  denote a valence VHS edge and  $m$  a conduction VHS edge where  $n$  and  $m$  run from  $-\infty$  to  $\infty$ . The transition between the  $n$  and  $m$  edge is of energy  $\Delta E_{nm} = \Delta_n + \Delta_m$  and accompanied by a change in isotropic band structure stress of

$$\begin{aligned} V_0\Delta\sigma_{0,nm} &= V_0\delta\sigma_0(\Delta_m) - V_0\delta\sigma_0(-\Delta_n) \\ &= -\frac{\alpha a_0}{\sqrt{3}t_0}\Delta E_{nm} \end{aligned} \quad (38)$$

where use of Eq. (27) was made. Hence, the expected strength of the response for a single electron (per unit cell) is linear in excitation energy and always negative, which mean the  $\gamma_0$  mode will always expand.

## X. CONCLUSIONS

In accordance with previous studies<sup>22–24,28,29</sup> our results predict a charge-induced quantum-mechanical change in the size of carbon nanotubes. Our decomposition of the total band structure stress into energy resolved band structure stresses yields a natural criterion for the discrimination of *bonding* and *anti-bonding* states that intuitively explains the observed quantum-mechanical response. We define the character of an orbital, bonding or anti-bonding, with respect to the  $\gamma_0$  mode, i.e. a uniform scaling of the system. It is the most natural mode since it describes simultaneous elongation of all bonds. The anisotropic  $\gamma_1$  mode, for example, conserves the overall volume in the limit of small distortions and represents a modulation of the radial and axial actuation modes that are otherwise dominated by the  $\gamma_0$  mode.

Beyond previous studies our results indicate, that additional functionalization has little influence on the actuation of metallic tubes. Since it is not yet possible to separate CNTs by chirality on a large scale, we expect that metallic CNTs dominate the overall behavior

because the band gap needs to be overcome in order to be able to charge semiconducting CNTs. Hence functionalization should have little influence on the expected response of a composite actuator.

In this article the Coulomb interaction of tubes in an electrolyte is introduced in a realistic manner. It leads to a strain that is symmetric in charge. This will average out the differences observed between tube chiralities within the quantum-mechanical response and lead to a more uniform actuation. In our work the capacity of the double-layer is independent of charge. This rather crude approximation is completely sufficient when regarding the actuation as a function of charge. Future work should focus on modeling the actuator including electron reservoirs which will require to capture the capacities of the individual components of the actuator. Hence for obtaining the actuator response as a function of applied voltage, the underlying double-layer model plays a crucial role. The total charge which can be brought onto a tube then also depends on the tube's quantum capacity. This quantity is linked to the density of states at the Fermi level<sup>70</sup>, and has been discussed in detail for gated CNT devices<sup>71,72</sup>. Nevertheless, the inclusion of Coulomb interaction allows quantitative predictions of the expected magnitude of the response which is of the order of 0.1%, comparable to piezo-actuators.

A simple consideration sheds some light on the major approximation made in this and previous works<sup>22–24,28,29</sup>, the assumption that the number of electrons on the system stays constant when the CNT is strained. Since for metallic CNTs the density of states per atom at the Fermi-level is independent of the CNT chirality, the tubes quantum capacitance (per atom) is given by  $C_q = e^2 g(\mu)$ . From Eq. (22) one obtains  $g^{-1}(\mu) = \frac{1}{4} l a_0 t_0 (\sqrt{3} - A \gamma_{\parallel})$  which depends on the axial strain  $\gamma_{\parallel}$ . The classical double-layer capacitance (per atom)  $C_{cl}$  as obtained from the simple capacitor model Eq. (37) saturates for large diameters and to linear order in  $\gamma_{\parallel}$  and  $\gamma_{\perp}$  at  $C_{cl} = \epsilon_r \epsilon_0 d^{-1} (1 + \gamma_0) A_C$  where  $d$  is the double-layer distance and  $A_C$  the area per carbon atom in the unstrained case. This leads to interfacial capacities (per interface area  $A_{int}$ ) of roughly  $C_q A_{int}^{-1} = 8 \mu\text{F cm}^{-2}$ ,  $C_{cl} A_{int}^{-1} = 11 \mu\text{F cm}^{-2}$  and a combined interfacial capacitance of  $C_{tot} A_{int}^{-1} = 4.5 \mu\text{F cm}^{-2}$  for water ( $d = 4 \text{ \AA}$  and  $\epsilon_r = 5$ ). These values are in good agreement with experimentally reported<sup>10,58</sup> values of 4–10  $\mu\text{F cm}^{-2}$ , which shows that such a simple model is already a reasonable approximation. Since both  $C_q$  and  $C_{cl}$  (per atom) increase with increasing  $\gamma_{\parallel}$  the total capacitance  $C_{tot} = (C_q^{-1} + C_{cl}^{-1})^{-1}$  of the CNT-double-layer system is strain dependent and no cancellation occurs. Thus, the results obtained here are valid for experiments in which the actuator is controlled *galvanostatically* where the influence of a change in capacitance is automatically compensated.

We also present first insights into possible mechanisms leading to photo-induced actuation. The model does not give absolute strains and stresses, however we expect these to be similar in magnitude to the charge-induced

case. Qualitatively, the tubes modulate intrinsic stresses in the polymer-nanotube composite which could trigger kinking of individual tubes, as proposed in Ref. 11. Future experiments should measure strains as function of irradiation wavelength. Our results predict that the response of a single excited electron should be proportional to the photon energy. Quantitative predictions of the expected intrinsic stresses could be obtained by combining our results with appropriate activation cross-sections and lifetimes of the expected excitations.

## Acknowledgments

Funding for L.P. and M.M. was provided by the BMBF (project ‘‘CaNaMAT’’) and the Fraunhofer Society (MaVo ‘‘CarNAk’’ and a sabbatical for M.M.). P.K. acknowledges funding by the Academy of Finland. Computations were carried out at Fraunhofer EMI, ITWM and IWM as well as at HLRS Stuttgart, and NIC Jülich.

## Appendix A: Next-nearest-neighbor $\pi$ -orbital model

A next-neighbor zone-folding model for the electronic structure of distorted CNTs was first given by Yang and Han<sup>27</sup> and later extended to next-nearest-neighbor hopping by Gartstein and co-workers<sup>28,29</sup>. We follow along a similar line and give a full derivation of the model since our notation and some approximations differ from the work of Gartstein.

The next-nearest-neighbor  $\pi$ -orbital Hamiltonian for graphene is given by

$$H = \begin{pmatrix} H_{11} & H_{12}^* \\ H_{12} & H_{11} \end{pmatrix} \quad (\text{A1})$$

where

$$H_{11} = 2u_a \cos \vec{k} \cdot \vec{a}_{12} + 2u_b \cos \vec{k} \cdot \vec{a}_2 + 2u_c \cos \vec{k} \cdot \vec{a}_1 \quad (\text{A2})$$

and

$$H_{12} = t_a + t_b \exp i \vec{k} \cdot \vec{a}_1 + t_c \exp i \vec{k} \cdot \vec{a}_2 \quad (\text{A3})$$

with  $\vec{a}_{12} = \vec{a}_1 - \vec{a}_2$ . Here  $\vec{a}_1$  and  $\vec{a}_2$  are the vectors of the graphene unit cell,  $t_a$ ,  $t_b$ , and  $t_c$  the nearest-neighbor hopping matrix elements and  $u_a$ ,  $u_b$  and  $u_c$  next-nearest-neighbor hopping matrix elements as defined in Fig. 10. Writing  $\vec{k} = x_1 \vec{b}_1 + x_2 \vec{b}_2$  in terms of the reciprocal lattice vectors  $\vec{b}_1$  and  $\vec{b}_2$  leads to two energy bands

$$\epsilon(x_1, x_2) = \tau(x_1, x_2) \pm \xi(x_1, x_2) \quad (\text{A4})$$

where the contribution due to nearest-neighbor hopping is given by

$$\xi^2(x_1, x_2) = t_a^2 + t_b^2 + t_c^2 + 2t_a t_b \cos x_1 + 2t_c t_a \cos x_2 + 2t_b t_c \cos(x_1 - x_2). \quad (\text{A5})$$

and the contribution due to next-nearest-neighbor hopping by

$$\tau(x_1, x_2) = -2u_a \cos(x_1 - x_2) - 2u_b \cos x_2 - 2u_c \cos x_1. \quad (\text{A6})$$

The bands touch where  $\xi^2(\vec{x})$  has its minimum. In the undistorted case (i.e.  $t_a = t_b = t_c$  and  $u_a = u_b = u_c$ ) these points are located at  $\vec{x}^{(0)} = (-2\pi/3, 2\pi/3)$  and  $\vec{x}^{(0)} = (2\pi/3, -2\pi/3)$ . We now approximate the next-nearest-neighbor contribution to be dispersionless and given by the value at  $\vec{x}^{(0)}$ , i.e.  $\tau = -u_a - u_b - u_c$ .

The nearest neighbor contribution  $\xi^2(x_1, x_2)$  is expanded around its *undistorted* minimum. An expansion up to *second* order is used to determine the new minimum, while a *fourth* order expansion is necessary to determine the curvature at the new minimum. Let  $\vec{x}' = \vec{x} - \vec{x}^{(0)}$  and expanding  $\cos$  up to fourth order in  $\xi^2(\vec{x})$ , i.e. using

$$\begin{aligned} \cos\left(x + \frac{2\pi}{3}\right) &= -\frac{1}{2} - \frac{\sqrt{3}}{2}x + \frac{x^2}{4} \\ &+ \frac{\sqrt{3}}{12}x^3 - \frac{x^4}{48} + \mathcal{O}(x^5) \end{aligned} \quad (\text{A7})$$

and

$$\begin{aligned} \cos\left(x + \frac{4\pi}{3}\right) &= -\frac{1}{2} + \frac{\sqrt{3}}{2}x + \frac{x^2}{4} \\ &- \frac{\sqrt{3}}{12}x^3 - \frac{x^4}{48} + \mathcal{O}(x^5) \end{aligned} \quad (\text{A8})$$

one finds for the second order expansion

$$\begin{aligned} \left(\xi^{(2)}\right)^2(x'_1, x'_2) &\approx t_a^2 + t_b^2 + t_c^2 - t_a t_b + t_b t_c + t_c t_a \\ &+ \frac{1}{2} t_a t_b (x'_1 + \sqrt{3})^2 \\ &+ \frac{1}{2} t_c t_a (x'_2 - \sqrt{3})^2 \\ &+ \frac{1}{2} t_b t_c (x'_1 - x'_2 - \sqrt{3})^2. \end{aligned} \quad (\text{A9})$$

For small changes in hopping matrix elements looking for the new minimum of  $\xi^{(2)}(\vec{x})$  within this expansion yields

$$\vec{x}'^{(0)} = \sqrt{3} \left\{ \frac{3}{t_a + t_b + t_c} \begin{pmatrix} t_c \\ t_b \end{pmatrix} - 1 \right\}, \quad (\text{A10})$$

which means the minimum is moved away from the  $K$ -point when the lattice is distorted. The curvature of  $\xi^2(\vec{x})$  at  $\vec{x}'^{(0)}$  determines the slopes of the Dirac cone in the  $\vec{k} \cdot \vec{p}$  approximation. This curvature is determined from the fourth order expansion of  $\xi(\vec{x})$  since it is constant in expression (A9). One finds

$$\begin{aligned} M_{11} &= \frac{\partial^2}{\partial x_1'^2} \left( \xi^{(4)} \right)^2(\vec{x}') \Big|_{\vec{x}'^{(0)}} \\ &= \frac{5}{2} t_b (t_a + t_c) \left\{ 1 - \frac{27 t_a t_c}{5(t_a + t_b + t_c)^2} \right\}, \end{aligned} \quad (\text{A11})$$

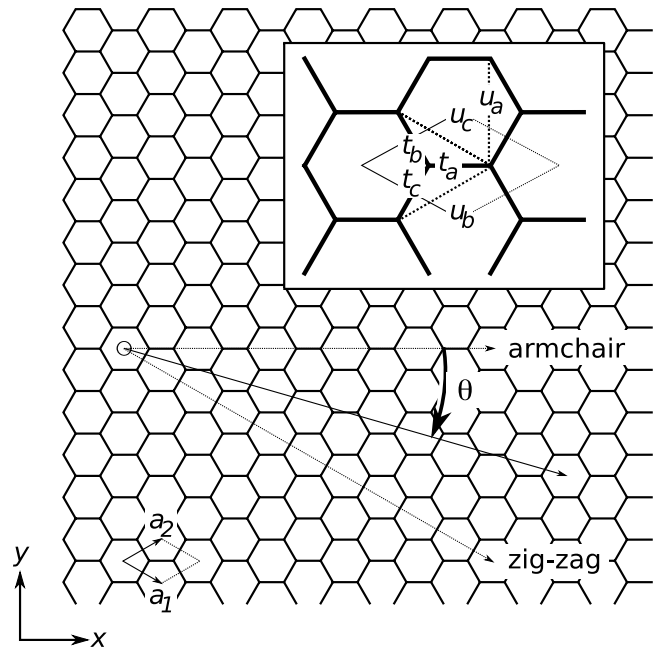


FIG. 10: Definition of the unit cell and the chiral angle in the graphene lattice. Inset: Notation of next-neighbor and next-nearest-neighbor hopping matrix elements.

$$\begin{aligned} M_{22} &= \frac{\partial^2}{\partial x_2'^2} \left( \xi^{(4)} \right)^2(\vec{x}') \Big|_{\vec{x}'^{(0)}} \\ &= \frac{5}{2} t_c (t_a + t_b) \left\{ 1 - \frac{27 t_a t_b}{5(t_a + t_b + t_c)^2} \right\} \end{aligned} \quad (\text{A12})$$

and

$$\begin{aligned} M_{12} &= \frac{\partial^2}{\partial x_1' \partial x_2'} \left( \xi^{(4)} \right)^2(\vec{x}') \Big|_{\vec{x}'^{(0)}} \\ &= \frac{5}{2} t_b t_c \left\{ 1 - \frac{27 t_a^2}{5(t_a + t_b + t_c)^2} \right\} \end{aligned} \quad (\text{A13})$$

where the hopping matrix elements  $t_a$ ,  $t_b$  and  $t_c$  need now be expressed in terms of bond lengths.

The hopping matrix elements are assumed to vary linearly as  $t_x = t_0 - \alpha \delta_x$  where  $\delta_x$  is the change in bond length due to distortion. The roll-up vector  $\vec{c} = n_1 \vec{a}_1 + n_2 \vec{a}_2$  is characterized by the tube circumference  $|\vec{c}|$  and the chiral angle  $\theta$  which is defined as the angle with respect to armchair tubes, i.e.  $\hat{c} = (\cos \theta, \sin \theta)$  in the coordinate system of Fig. 10. The matrix

$$\underline{R}(\theta) = \begin{pmatrix} \cos \theta & \sin \theta \\ -\sin \theta & \cos \theta \end{pmatrix} \quad (\text{A14})$$

rotates the roll-up vector onto the  $x$ -axis. Thus for isotropic  $\gamma_0$ , anisotropic  $\gamma_1$  and torsional  $\eta$  deformation the transformation matrix is given by

$$\underline{T} = \underline{R}^{-1}(\theta) \begin{pmatrix} \gamma_0 - \gamma_1 & \eta \\ \eta & \gamma_0 + \gamma_1 \end{pmatrix} \underline{R}(\theta) \quad (\text{A15})$$

which can be rotated onto the basis vectors of the deformed graphene and nanotube unit cell. The individual next-neighbor bond length  $l_x$  are given by

$$l_a = \frac{1}{3} |\vec{a}_1^T + \vec{a}_2^T|, \quad l_b = \frac{1}{3} |2\vec{a}_1^T - \vec{a}_2^T| \quad (\text{A16})$$

and

$$l_c = \frac{1}{3} |\vec{a}_1^T - 2\vec{a}_2^T| \quad (\text{A17})$$

where the superscript  $T$  denotes deformed unit cell vectors, i.e.  $\vec{x}^T = (1 + \underline{T})\vec{x}$ . Expanding to linear order in  $\gamma_0$ ,  $\gamma_1$  and  $\eta$  the change in bond length becomes

$$\delta_x = l_x^{(0)} \begin{pmatrix} \cos \phi_x/2 \\ \sin \phi_x/2 \end{pmatrix} \underline{T} \begin{pmatrix} \cos \phi_x/2 \\ \sin \phi_x/2 \end{pmatrix} \quad (\text{A18})$$

$$= \frac{1}{2} l_x^{(0)} \text{tr} \{ \underline{T} (1 + \underline{R}(\phi_x)) \} \quad (\text{A19})$$

where  $\phi_a = 0$ ,  $\phi_b = -2\pi/3$  and  $\phi_c = 2\pi/3$  is the rotation angle of the respective bond relative to the  $x$ -axis and  $l_x^{(0)} = a_0/\sqrt{3}$  the equilibrium bond length. Now the band energy can be written as the quadratic form

$$\xi^2(\vec{x}') = \frac{1}{2} \vec{x}'^T \underline{M} \vec{x}' \quad (\text{A20})$$

with  $\underline{M}$  being a symmetric matrix with coefficients given by equations (A11) to (A13). The coefficients of  $\underline{M}$  are now computed up to linear order in bond lengths, i.e.

$$\frac{M_{11}}{t_0^2} = 2 - \frac{4A}{a_0} \delta_b = 2 - \frac{2}{\sqrt{3}} A \text{tr} \{ \underline{T} (1 + \underline{R}(\phi_b)) \}, \quad (\text{A21})$$

$$\frac{M_{22}}{t_0^2} = 2 - \frac{4A}{a_0} \delta_c = 2 - \frac{2}{\sqrt{3}} A \text{tr} \{ \underline{T} (1 + \underline{R}(\phi_c)) \} \quad (\text{A22})$$

and

$$\begin{aligned} \frac{M_{12}}{t_0^2} &= -1 + \frac{2A}{a_0} (-\delta_a + \delta_b + \delta_c) \\ &= -1 + \frac{1}{\sqrt{3}} A \text{tr} \{ \underline{T} (1 - 2\underline{R}(\phi_a)) \} \end{aligned} \quad (\text{A23})$$

with  $A = \alpha a_0/t_0$ . Furthermore,  $\underline{R}(\phi_a) + \underline{R}(\phi_b) + \underline{R}(\phi_c) = 0$  has been used. This can be used to write the coefficient matrix as

$$\underline{M} = \underline{B}^t \underline{R}^t \underline{K} \underline{R} \underline{B} \quad (\text{A24})$$

with

$$\underline{K} = \frac{a_0^2 t_0^2}{2} \begin{pmatrix} 3 - 2\sqrt{3}A(\gamma_0 - \gamma_1) & -\sqrt{3}A\eta \\ -\sqrt{3}A\eta & 3 - 2\sqrt{3}A(\gamma_0 + \gamma_1) \end{pmatrix} \quad (\text{A25})$$

where the superscript  $t$  is the matrix transpose and  $\underline{B} = \underline{A}^{-1}$  are the reciprocal basis vectors. In order to express this equation in  $k$ -space, the vector  $\vec{k} = (k_\perp, k_\parallel)$  needs to

be rotated onto the tube's system by applying  $\underline{R}^{-1}$ . One finds

$$\vec{x} = \underline{A} \underline{R}^{-1} \vec{k} \quad (\text{A26})$$

and the dispersion relation in  $k$ -space becomes

$$\epsilon^2(\vec{k}) = \frac{1}{2} \vec{k} \underline{K} \vec{k} = v_\parallel^2 k_\parallel^2 + v_\perp^2 k_\perp^2 \quad (\text{A27})$$

where terms proportional to  $k_\parallel k_\perp$  have been absorbed by shifting  $k_\parallel$ . The effective Fermi velocities now become

$$\begin{aligned} v_\parallel &= \left\{ \frac{a_0^2 t_0^2}{4} \left( 3 - 2\sqrt{3}A(\gamma_0 + \gamma_1) \right) \right\}^{\frac{1}{2}} \\ &\approx \frac{a_0 t_0}{2} \left( \sqrt{3} - A(\gamma_0 + \gamma_1) \right) \end{aligned} \quad (\text{A28})$$

and

$$\begin{aligned} v_\perp &= \left\{ \frac{a_0^2 t_0^2}{4} \left( 3 - 2\sqrt{3}A(\gamma_0 - \gamma_1) \right) \right\}^{\frac{1}{2}} \\ &\approx \frac{a_0 t_0}{2} \left( \sqrt{3} - A(\gamma_0 - \gamma_1) \right). \end{aligned} \quad (\text{A29})$$

Furthermore, the minimum of  $\epsilon^2(\vec{x})$  moves to  $\vec{k}^{(0)} = \underline{R} \underline{B}^T \vec{x}^{(0)}$ , giving

$$\vec{k}^{(0)} a_0 = \begin{pmatrix} \gamma_1 \sin 3\theta - \eta \cos 3\theta \\ \gamma_1 \cos 3\theta + \eta \sin 3\theta \end{pmatrix} A. \quad (\text{A30})$$

## Appendix B: Solution of Poisson's equation for the charged cylinder

The Fourier-transform of the cylinder's density Eq. (35) is given by

$$V \rho(\vec{G}) = \int d^3 r \rho(\vec{r}) e^{i\vec{G} \cdot \vec{r}} \quad (\text{B1})$$

$$= Q \delta_{G_z, 0} \int d^2 r e^{i\vec{G} \cdot \vec{r}} \quad (\text{B2})$$

$$\times \left\{ \frac{\delta(\sqrt{x^2 + y^2} - r_0)}{2\pi r_0} - \frac{1}{l_x l_y} \right\}. \quad (\text{B3})$$

In cylindrical coordinates and after carrying out the integration over  $r$  this yields

$$V \rho(\vec{G}) = Q \delta_{G_z, 0} \left\{ \frac{1}{2\pi} \int_0^{2\pi} d\varphi e^{i|\vec{G}| r_0 \cos \varphi} - \delta_{G_x, 0} \delta_{G_y, 0} \right\}, \quad (\text{B4})$$

where the integral gives rises to a Bessel-function of the first kind and zeroth order  $J_0$ , i.e.

$$2\pi J_0(|x|) = \int_0^{2\pi} d\varphi e^{ix \cos \varphi}. \quad (\text{B5})$$

The  $\vec{G} = 0$  term of the Bessel-function cancels the corresponding one from the 3D-jellium background. The density in reciprocal space is thus given by

$$V\rho(\vec{G}) = \begin{cases} QJ_0(|\vec{G}|r_0) & \text{if } G_z = 0; G_x, G_y \neq 0 \\ 0 & \text{else} \end{cases} \quad (\text{B6})$$

and the electrostatic potential  $\phi$  is found by  $\rho(\vec{G}) = G^2\phi(\vec{G})$ . Equation (36) constitutes the back transformation into real space by direct summation.

- 
- \* Email address: lars.pastewka@iwm.fraunhofer.de  
† Email address: michael.moseler@iwm.fraunhofer.de
- <sup>1</sup> S. Iijima and T. Ichihashi, *Nature* **363**, 603 (1993).
  - <sup>2</sup> S. Iijima, *Nature* **354**, 56 (1991).
  - <sup>3</sup> J. Gao, M.E. Itkis, A. Yu, E. Bekyarova, B. Zhao, and R.C. Haddon, *J. Am. Chem. Soc.* **127**, 3847 (2005).
  - <sup>4</sup> T. Laha, A. Agarwal, T. McKechnie, and S. Seal, *Mater. Sci. Eng. A* **381**, 249 (2004).
  - <sup>5</sup> S. Guo, R. Sivakumar, and Y. Kagawa, *Adv. Eng. Mater.* **9**, 84 (2007).
  - <sup>6</sup> M.P. Anantram and F. Léonard, *Rep. Prog. Phys.* **69**, 507 (2006).
  - <sup>7</sup> A. M. Fennimore, T. D. Yuzvinsky, W.-Q. Han, M. S. Fuhrer, J. Cumings, and A. Zettl, *Nature* **424**, 408 (2003).
  - <sup>8</sup> P. Poncharal, Z. L. Wang, D. Ugarte, and W. A. de Heer, *Science* **283**, 1513 (1999).
  - <sup>9</sup> V. H. Ebron, Z. Yang, D. J. Seyer, M. E. Kozlov, J. Oh, H. Xie, J. Razal, L. J. Hall, J. P. Ferraris, A. G. MacDiarmid, et al., *Science* **311**, 1580 (2006).
  - <sup>10</sup> R. H. Baughman, C. Cui, A. A. Zakhidov, Z. Iqbal, J. N. Barisci, G. M. Spinks, G. G. Wallace, A. Mazzoldi, D. D. Rossi, A. G. Rinzler, et al., *Science* **284**, 1340 (1999).
  - <sup>11</sup> S. V. Ahir and E. M. Terentjev, *Nat. Mater.* **4**, 491 (2005).
  - <sup>12</sup> A.Z. Hartman, M. Jouzi, R.L. Barnett, and J.M. Xu, *Phys. Rev. Lett* **92**, 236804 (2004).
  - <sup>13</sup> C. Li, E.T. Thostenson, and T.-W. Chou, *Compos. Sci. Technol.* **68**, 1227 (2008).
  - <sup>14</sup> Y. Zhang and S. Iijima, *Phys. Rev. Lett.* **82**, 3472 (1999).
  - <sup>15</sup> S. Lu, S. V. Ahir, E. M. Terentjev, and B. Panchapakesan, *Appl. Phys. Lett.* **91**, 103106 (2007).
  - <sup>16</sup> S. Lu and B. Panchapakesan, *Nanotechnology* **18**, 305502 (2007).
  - <sup>17</sup> S. Lu, Y. Liu, N. Shao, and B. Panchapakesan, *Nanotechnology* **18**, 065501 (2007).
  - <sup>18</sup> S. V. Ahir, E. M. Terentjev, S. X. Lu, and B. Panchapakesan, *Phys. Rev. B* **76**, 165437 (2007).
  - <sup>19</sup> S. V. Ahir and E. M. Terentjev, *Phys. Rev. Lett.* **96**, 133902 (2006).
  - <sup>20</sup> S. V. Ahir, A. M. Squires, A. R. Tajbakhsh, and E. M. Terentjev, *Phys. Rev. B* **73**, 085420 (2006).
  - <sup>21</sup> H.-J. Butt, K. Graf, and M. Kappl, *Physics and Chemistry of Interfaces* (Wiley-VCH, 2003).
  - <sup>22</sup> G. Sun, J. Kürti, M. Kertesz, and R. H. Baughman, *J. Phys. Chem. B* **107**, 6924 (2003).
  - <sup>23</sup> M. Verissimo-Alves, B. Koiller, H. Chacham, and R. B. Capaz, *Phys. Rev. B* **67**, 161401(R) (2003).
  - <sup>24</sup> G. Sun, J. Kürti, M. Kertesz, and R. H. Baughman, *J. Am. Chem. Soc.* **124**, 15076 (2002).
  - <sup>25</sup> J. W. Mintmire and C. T. White, *Phys. Rev. Lett.* **81**, 2506 (1998).
  - <sup>26</sup> C. T. White and J. W. Mintmire, *Nature* **394**, 29 (1998).
  - <sup>27</sup> L. Yang and J. Han, *Phys. Rev. Lett.* **85**, 154 (2000).
  - <sup>28</sup> Y. N. Gartstein, A. A. Zakhidov, and R. H. Baughman, *Phys. Rev. B* **68**, 115415 (2003).
  - <sup>29</sup> Y. N. Gartstein, A. A. Zakhidov, and R. H. Baughman, *Phys. Rev. Lett.* **89**, 045503 (2002).
  - <sup>30</sup> W. Guo and Y. Guo, *Phys. Rev. Lett.* **91**, 115501 (2003).
  - <sup>31</sup> C. Li and T.-W. Chou, *Carbon* **45**, 922 (2007).
  - <sup>32</sup> C.-Y. Li and T.-W. Chou, *Nanotechnology* **17**, 4624 (2006).
  - <sup>33</sup> J. Weissmüller, R.N. Viswanath, D. Kramer, P. Zimmer, R. Wurschum, and H. Gleiter, *Science* **300**, 312 (2003).
  - <sup>34</sup> D. Kramer and J. Weissmüller, *Surf. Sci.* **601**, 3042 (2007).
  - <sup>35</sup> J. Weissmüller and D. Kramer, *Langmuir* **21**, 4592 (2005).
  - <sup>36</sup> Y. Umeno, C. Elsässer, B. Meyer, P. Gumbsch, M. Nothacker, J. Weissmüller, and F. Evers, *Europhys. Lett.* **78**, 13001 (2007).
  - <sup>37</sup> F. Weigend, F. Evers, and J. Weissmüller, *Small* **2**, 1497 (2006).
  - <sup>38</sup> M. Finnis, *Interatomic Forces in Condensed Matter* (Oxford University Press, 2004).
  - <sup>39</sup> By appropriately choosing  $\mathcal{M}_x$  the forces on individual atoms are also included in that definition of pressure. Hence, the framework developed in this article also provides a definition of orbital-resolved forces which can be used to study charge induced relaxations.
  - <sup>40</sup> M. Arroyo and T. Belytschko, *Phys. Rev. B* **69**, 115415 (2004).
  - <sup>41</sup> R. M. Martin, *Electronic Structure* (Cambridge University Press, 2004).
  - <sup>42</sup> J. W. Mintmire, B. I. Dunlap, and C. T. White, *Phys. Rev. Lett.* **68**, 631 (1992).
  - <sup>43</sup> P. R. Wallace, *Phys. Rev.* **71**, 622 (1947).
  - <sup>44</sup> R. Saito, M. Fujita, G. Dresselhaus, and M. S. Dresselhaus, *Phys. Rev. B* **46**, 1804 (1992).
  - <sup>45</sup> N. Hamada, S.I. Sawada, and A. Oshiyama, *Phys. Rev. Lett.* **68**, 1579 (1992).
  - <sup>46</sup> D. Porezag, Th. Frauenheim, T. Köhler, G. Seifert, and R. Kaschner, *Phys. Rev. B* **51**, 12947 (1995).
  - <sup>47</sup> We use the HOTBIT code; P. Koskinen and V. Mäkinen, submitted.
  - <sup>48</sup> M. Elstner, D. Porezag, G. Jungnickel, J. Elsner, M. Haugk, Th. Frauenheim, S. Suhai, and G. Seifert, *Phys. Rev. B* **58**, 7260 (1998).
  - <sup>49</sup> J. M. Soler, E. Artacho, J. D. Gale, A. García, J. Junquera, P. Ordejón, and D. Sánchez-Portal, *J. Phys.: Condens. Mat.* **14**, 2745 (2002).
  - <sup>50</sup> R. Saito, G. Dresselhaus, and M. S. Dresselhaus, *Physical Properties of Carbon Nanotubes* (Imperial College Press, 1998).
  - <sup>51</sup> P. Koskinen, H. Hakkinen, G. Seifert, S. Sanna, Th. Frauenheim, and M. Moseler, *New J. Phys* **8**, 9 (2006).
  - <sup>52</sup> W. Kohn and L. J. Sham, *Phys. Rev.* **140**, A1133 (1965).
  - <sup>53</sup> N. Troullier and J. L. Martins, *Phys. Rev. B* **43**, 1993 (1991).
  - <sup>54</sup> We checked against PBE calculations with no noticeable

difference in the obtained results.

- <sup>55</sup> J. P. Perdew and A. Zunger, Phys. Rev. B **23**, 5048 (1981).
- <sup>56</sup> J. P. Perdew, K. Burke, and M. Ernzerhof, Phys. Rev. Lett. **77**, 3865 (1996).
- <sup>57</sup> E. Bitzek, P. Koskinen, F. Gähler, M. Moseler, and P. Gumbsch, Phys. Rev. Lett. **97**, 170201 (2006).
- <sup>58</sup> H. Gerischer, R. McIntyre, D. Scherson, and W. Storck, J. Phys. Chem. **91**, 1930 (1987).
- <sup>59</sup> D. B. Mawhinney, V. Naumenko, A. Kuznetsova, J. T. Yates Jr., J. Liu, and R. E. Smalley, Chem. Phys. Lett. **324**, 213 (2000).
- <sup>60</sup> A. Hirsch, Angew. Chem. Int. Ed. **41**, 1853 (2002).
- <sup>61</sup> J. D. Jackson, *Classical Electrodynamics* (John Wiley & Sons, 1999).
- <sup>62</sup> M. W. Deem, J. M. Newsam, and S. K. Sinha, J. Phys. Chem. **94**, 8356 (1990).
- <sup>63</sup> P. J. Stiles, J. B. Hubbard, and R. F. Kayser, J. Chem. Phys. **77**, 6189 (1982).
- <sup>64</sup> J. Cumings and A. Zettl, Science **289**, 602 (2000).
- <sup>65</sup> A.N. Kolmogorov and V.H. Crespi, Phys. Rev. Lett. **85**, 4727 (2000).
- <sup>66</sup> F. Wang, G. Dukovic, L. E. Brus, and T. F. Heinz, Science **308**, 838 (2005).
- <sup>67</sup> E. Malić, M. Hirtschulz, F. Milde, A. Knorr, and S. Reich, Phys. Rev. B **74**, 195431 (2006).
- <sup>68</sup> S. V. Goupalov, Phys. Rev. B **72**, 195403 (2005).
- <sup>69</sup> P. N. D'yachkov and H. Hermann, J. Appl. Phys. **95**, 399 (2004).
- <sup>70</sup> M. Büttiker, J. Phys.: Condens. Mat. **5**, 9361 (1993).
- <sup>71</sup> P. Pomorski, L. Pastewka, C. Roland, H. Guo, and J. Wang, Phys. Rev. B **69**, 115418 (2004).
- <sup>72</sup> P. Pomorski, C. Roland, H. Guo, and J. Wang, Phys. Rev. B **67**, 161404(R) (2003).